Trailing-edge noise from the scattering of spanwise-coherent structures

Alex Sano,* Leandra I. Abreu,† and André V. G. Cavalieri
Divisão de Engenharia Aeronáutica, Instituto Tecnológico de Aeronáutica, São José dos Campos, SP, Brazil

William R. Wolf
Faculdade de Engenharia Mecânica, Universidade Estadual de Campinas, Campinas, SP, Brazil

(Received 7 November 2018; published 12 September 2019)

A large-eddy simulation of turbulent, compressible flow around a NACA 0012 airfoil at zero angle of attack and Mach number 0.115 is used to study mechanisms of trailing-edge noise. The boundary layers at both sides of the airfoil have a forced transition near the airfoil leading edge, and are turbulent near the trailing-edge. Flow-acoustic correlations and spectral (frequency-domain) proper orthogonal decomposition (SPOD) are used to evaluate turbulent structures that are relevant for the radiated sound. Homogeneity in the spanwise direction allows application of a Fourier decomposition in span prior to both correlations and SPOD. It is known that acoustic theory, based on an analysis of the tailored Green's function modeling trailing-edge scattering, shows that only spanwise wave numbers k_z satisfying $k_z < k$, where k is the acoustic wave number, lead to radiated sound; two-dimensional disturbances ($k_z = 0$) always satisfy this criterion, and thus spanwise-coherent structures are expected to be important for trailing-edge noise. Analysis of turbulence statistics of the boundary layer close to the trailing edge shows that the well-known, dominant streaky structures have $k_z > k$ and thus should not contribute to the radiated sound. To investigate this further using simulation data, flow-acoustic correlations are obtained using either the standard two-point analysis or considering two-dimensional disturbances in velocity and pressure fields, and results show significant correlation coefficients (of about 0.5) once two-dimensional disturbances near the trailing edge are isolated. A further increase of correlation peaks (up to 0.7) is obtained once the antisymmetric parts of the fields is considered, reflecting the classical antisymmetric nature of trailing-edge scattering. SPOD is then used for frequencies around the peak radiated sound to examine the structure of two-dimensional disturbances in the trailing-edge region and their contribution to radiated sound. Leading SPOD modes show coherent hydrodynamic waves propagating from the region of boundary-layer tripping toward the trailing edge, characterizing a noncompact source akin to wave packets seen in turbulent jets. These leading SPOD modes have significant contribution to the radiated sound, as two modes lead to 50% of the acoustic intensity for the lower studied frequencies. The present results point to the scattering of spanwise-coherent boundary-layer structures as the dominant mechanism of trailing-edge noise in this flow.

DOI: 10.1103/PhysRevFluids.4.094602

I. INTRODUCTION

Noise emitted by airfoils, wings, and blades occurs due to the interaction of turbulence with the neighboring solid surfaces. At low angles of attack and high Reynolds numbers, boundary layers

*sano@ita.br
†leandraabreu13@gmail.com

around an airfoil surface are often turbulent, and the interaction of advecting turbulence with an edge is referred to as trailing-edge noise [1], which is a result of the trailing edge inducing an abrupt change of boundary conditions for pressure and/or velocity (Moreau and Roger [2]). Trailing-edge noise is the dominant sound-source mechanism for an airfoil at low angle of attack, as shown by Lockard and Lilley [3], and there are thus several applications where this phenomenon is relevant, such as for the design of low-noise aerodynamic profiles, rotor blades, and fans.

The relevance of trailing-edge noise was recognized early by Ffowcs Williams and Hall [4], who showed theoretically, using a tailored Green's function in Lighthill's analogy, that a trailing edge scatters the neighboring turbulent fluctuations, leading to sound radiation that is much more significant than what is found for free turbulence. Unlike sound emission by compact surfaces, which tends to be dominated by lift fluctuations as shown by Curle [5], trailing-edge noise approaches the noncompact surface limit; accordingly, airfoils are modeled by Ffowcs Williams and Hall as a half plane with eddies (modeled as compact quadrupole) at the vicinity of its edge.

Follow-up modeling work by Amiet [6,7] also dealt with a scattering problem related to trailing-edge noise, this time considering that a surface pressure spectrum is incident at the edge. The basic assumption is that a model spectrum obtained empirically for zero-pressure-gradient turbulent boundary layers [8] is considered as an incident pressure load at the edge, and must be balanced by the scattered pressure such that the boundary conditions of the problem are satisfied. This became a common assumption in trailing-edge noise models for more complex cases such as backscattering by the leading edge [9], scattering by elastic plates [10] or by serrated trailing edges [11]. The simplification of "frozen" boundary-layer turbulence, independent of the presence of the edge, may be unrealistic; in particular, in the trailing-edge region adverse pressure gradients occur, which leads to changes in turbulent boundary-layer structures [12]. However, the difficulty in obtaining cross-spectral densities of the surface pressure in experiments often leads to the use of the simple model given by Corcos; a notable exception is the work of Brooks and Hodgson [13], who obtained convection velocities and coherence lengths in both streamwise and spanwise direction for turbulent boundary layers around an airfoil.

Computations such as direct numerical simulations (DNS) or large-eddy simulations (LES) may help circumvent such issues by providing full data of flow fluctuations around airfoils. Oberai *et al.* [14] confirmed, using an LES, that the source of acoustic noise is largely concentrated on trailing edge. Sandberg *et al.* [15] compared DNS results to the theory of Amiet [7], with good agreement; in this study, the pressure difference between lower and upper surfaces was taken from the simulation, and used as an input to the theoretical model. Sandberg and Sandham [16] employed DNS to show that two-dimensional theory for low frequencies predicts the far field acoustic pressure due the significant spanwise coherence of pressure disturbances, showing that in this case the noise generation is mainly two-dimensional. The availability of all flow fluctuations in simulation data also enables studies of flow-acoustic correlations, to determine the most relevant phenomena for sound radiation; a recent example was presented by Jones *et al.* [17].

Nonetheless, the turbulence structures relevant to trailing-edge noise remain to be determined. In the last decades, turbulent wall-bounded flows have seen substantial progress in the eduction and modeling of coherent turbulent structures. Common features of turbulent boundary layers are the near-wall streaks [18,19] and large- or very-large-scale motions [20,21]; such structures have been modeled dynamically using a wave description to turbulent fluctuations, using the resolvent operator related to the linearized Navier-Stokes system [22,23], which is relevant to the present study. However, works on turbulent wall-bounded flows are often concerned with aerodynamic quantities, such as the wall friction coefficient, and the most energetic structures in a turbulent flow might not be the most relevant ones for acoustic radiation. For trailing-edge noise, simulations of Ref. [24] have shown that the boundary layer upstream of the trailing edge is dominated by streaky structures, whereas the wake presents turbulent structures that become more coherent in the spanwise direction. Spanwise coherence is important for the trailing-edge noise problem, since only spanwise wavelengths larger than the acoustic wavelength lead to acoustic scattering [25]. With this in mind, the present work uses flow simulation data to study in more detail the

relevant sound-production mechanisms in the flow, in particular with a view to extracting the relevant turbulent scales to the trailing-edge noise problem, which may be different to the mentioned turbulent structures dominating velocity fluctuations in the boundary layer and wake.

For that matter, another useful data-driven approach is proper orthogonal decomposition (POD) [26]. POD is a quantitative method often applied with instantaneous fields from experimental data, but also from detailed computations such as DNS or LES to identify coherent structures in turbulent flows. POD provides a basis for the modal decomposition as an ensemble of functions, called POD modes, which are extracted from a set of data and capture the most energetic structures. Therefore, if the dynamics of the flow have a few predominant flow structures, then the data can often be well represented using just some of the first modes, which will then reflect the dominant flow structures. This method has been successfully used in various types of flows, such as mixing layers [27], jets [28], channel flows [29], cylinder wakes [30], and boundary layers [31]. More recently, POD in the frequency domain, also labeled as spectral POD (SPOD) [32], has been used to obtain coherent structures in turbulent jets [33,34]; its success in the eduction of coherent structures can be attributed to its relationship to the modal decomposition obtained in resolvent analysis [35]. In a recent work, Sanjose *et al.* [36] used SPOD to analyze a transitional flow in an airfoil, showing that interaction between coherent structures and instabilities are associated with acoustic wave scattering in the trailing edge. The dominant acoustic energy was related to two-dimensional modes. Due to its useful properties, SPOD will be used in this work to study turbulent structures relevant for trailing-edge noise. Differently from the flow studied by Sanjose *et al.* [36], which was dominated by Tollmien-Schlichting waves marking the initial stage of transition to turbulence, we focus on a case with developed turbulent boundary layers, with a higher Reynolds number.

In the present study, an LES of the compressible flow over a NACA 0012 airfoil at zero angle of attack with Mach number $M_\infty = 0.115$ and chord-based Reynolds number $\mathrm{Re}_c = 408\,000$ is studied using flow-acoustic correlations and SPOD. The homogeneity in the spanwise direction allows a preliminary Fourier decomposition, and the two-dimensional part of the flow field and radiated sound is of particular concern due to the two-dimensional nature of the radiated sound. The database is used to calculate flow-acoustic correlations to examine the relevant fluid motions and coherent structures related to acoustic radiation, while SPOD allows an identification of the most energetic structures for specific frequencies. SPOD modes are extended to the acoustic field, and the contribution of the leading modes to trailing-edge noise is assessed.

This paper is organized as follows. In Sec. II, the LES database performed by Wolf *et al.* [37] is briefly described. Section III presents some results in terms of turbulence statistics such as spectra, with an analysis of the structures that are expected to be relevant for sound radiation. In Sec. IV flow-acoustic correlations are performed, highlighting important regions for trailing-edge noise and clarifying the role of spanwise-coherent fluctuations. Section V presents details about the SPOD technique including an analysis of the SPOD modes obtained from the database and their relationship to the radiated sound. The paper is completed with conclusions in Sec. VI.

II. NUMERICAL SIMULATION

The large-eddy simulations (LES) in this work are taken from Wolf *et al.* [37]. Simulations are carried out for a flow around a NACA 0012 airfoil at zero angle of attack. Time-resolved data is available for all points in the grid. In what follows we summarize some of the simulation characteristics. To perform the numerical simulation two different grids were used. The first allows accurate resolution of the airfoil boundary layer. This grid is a body-fitted O-grid block composed by $1536 \times 125 \times 128$ nodes [Fig. 1(b)]. The second grid is more appropriate for acoustic waves emanating from the airfoil. This grid is a Cartesian background grid block and it is composed by $896 \times 511 \times 64$ nodes [Fig. 1(a)]. The trailing edge of the airfoil is rounded, as shown in Fig. 1(c). In addition, the grids are coupled using fourth order Hermitian interpolation ensuring numerical stability; more details about the implementation can be found in Ref. [38].

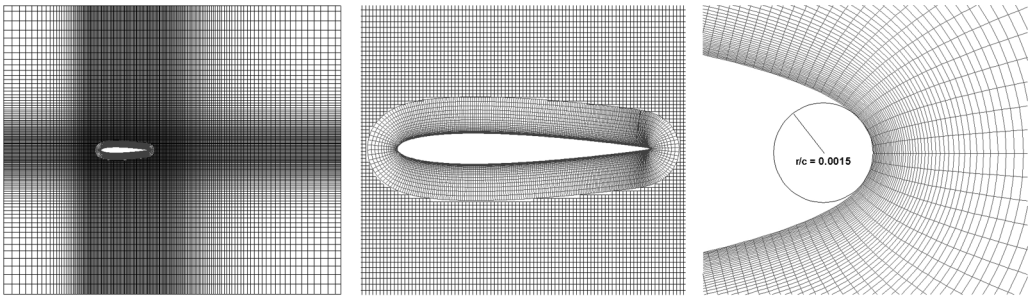

FIG. 1. Mesh details: (a) full view of Cartesian grid composed by $896 \times 511 \times 64$ nodes; (b) body-fitted O-grid block composed by $1536 \times 125 \times 128$ nodes; (c) detailed rounded trailing edge. Panels (a) and (b) show only 1 in every 4 points of the grid.

The simulated flow is at chord-based Reynolds number $\mathrm{Re}_c = 4.08 \times 10^5$ and at Mach number $M_\infty = 0.115$. To force transition to turbulence in the boundary layer, a boundary layer trip was simulated using artificial blowing and suction between $x/c = 0.15$ and 0.2, where x is the streamwise coordinate and c is the airfoil chord. The remaining Cartesian coordinates y and z are in the chord-normal and spanwise directions, respectively. The origin of the coordinate system is at the leading edge of the airfoil. Blowing and suction are applied at both upper and lower surfaces of the airfoil. The boundary layers near the trailing edge are turbulent, as seen in Ref. [37] by comparisons of mean flow and fluctuation profiles with DNS and experimental results.

The numerical simulation uses the dynamic subgrid model formulation of Ref. [39] to include the effects of unresolved turbulent scales [37]. The convergence of statistics from the numerical simulation was verified, and the total computation time of $t_0/c = 15.98$ (with initial transients discarded from the time series) was considered to be sufficient. Here a_0 refers to the ambient speed of sound.

Figure 2 shows a comparison of sound pressure level between the current numerical prediction and experimental data for an observer positioned at $x = c$, $y = 7.9c$ and midspan; the angular frequency ω is made nondimensional by using a Helmholtz number $\mathrm{He} = \omega c/a_0$. A corresponding Strouhal number $\mathrm{St} = fc/U_\infty$ can be obtained as $\mathrm{St} = \mathrm{He}/(2\pi M_\infty)$. The present numerical predictions show close agreement with the experimental measurements. A small peak can be seen in Fig. 2 for $\mathrm{He} \approx 12$, which can be associated with the possible presence of vortex shedding due to trailing-edge bluntness. Further validation results can be found in Ref. [37].

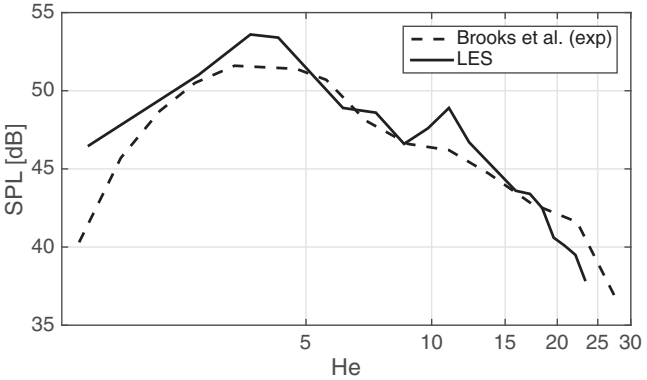

FIG. 2. Sound pressure level at observer location $x = c$, $y = 7.9c$ and midspan.

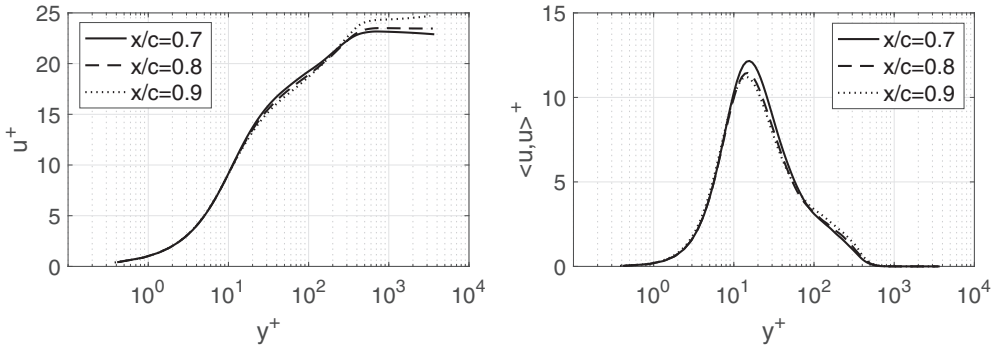

(a) (b)

FIG. 3. (a) The base flow and (b) mean square streamwise velocity at three different stations of the profile: $x/c = 0.7$, $x/c = 0.8$, and $x/c = 0.9$.

In the present study, focus is given on the frequency of the highest peak, He ≈ 4.95. We also analyze the neighboring He ≈ 7.42, the frequency correspondent to the second small peak He ≈ 12.37 and higher frequencies He ≈ 17.32 and He ≈ 22.26. These values are chosen based on the frequency discretization used in Welch's method to obtain power and cross-spectral densities.

III. TURBULENCE STATISTICS AND SPECTRA

The mean streamwise velocity profiles (u^+) and the variance profile ($\langle u, u\rangle^+$) in inner scaling are show in Figs. 3(a) and 3(b), respectively. The inner scaling is obtained by considering the friction velocity u_τ as a reference value, and the viscous lengthscale ν/u_τ as the reference length; the $+$ superscript refers to this inner scaling. The mean streamwise velocity profiles show the expected shape with a linear increase in the viscous sub-layer and a logarithmic overlap region growing for downstream stations due to the increase of the Reynolds number based on boundary-layer thickness. For the considered positions, the variance profiles have the expected pattern typical of boundary layers, with a peak in the buffer layer at $y^+ = 15$.

To visualize turbulent structures present in the boundary layer, Figs. 4(a) and 4(b) show the streamwise velocity fluctuations in two wall-parallel planes at $y^+ \approx 15$ and 100, respectively, positions that are representative of the buffer and log layers. The contour amplitude spans -0.5 to $+0.5$ standard deviations of the respective field shown. The dominant structures have the characteristic streaky shape, elongated in the streamwise direction. The buffer-layer streaks have a characteristic spanwise wavelength of $\lambda_z^+ \approx 100$, whereas log-layer structures have larger spanwise wavelengths. These features are standard in wall-bounded turbulent flows (see, for instance, Ref. [40]).

Such streaky structures are clearly dominant in the turbulent boundary layer over the airfoil. However, as discussed in the Introduction, spanwise-coherent disturbances are expected to be more relevant for trailing-edge noise [25]. To highlight spanwise-coherent disturbances of the raw velocity fields $u(x, z)$ at $y^+ \approx 15$ and $y^+ \approx 100$, both fields are spanwise averaged, and results are shown in Figs. 5(a) for $y^+ \approx 15$ and 5(b) for $y^+ \approx 100$. The spanwise-averaged fields have a broadband wave behavior. They are not apparent in the visualizations of the full velocity fields in Fig. 4, due to the low amplitude of spanwise-averaged fluctuations, which are an order of magnitude lower than the dominant streaky fluctuations. The turbulent boundary layer around the airfoil therefore comprises spanwise-coherent waves, which may be relevant for trailing-edge noise despite their low amplitude. This will be further explored next.

The premultiplied spanwise energy spectra of streamwise velocity fluctuations are shown in Fig. 6 for three different stations of the profile: $x/c = 0.7$, $x/c = 0.8$, and $x/c = 0.9$. A maximum

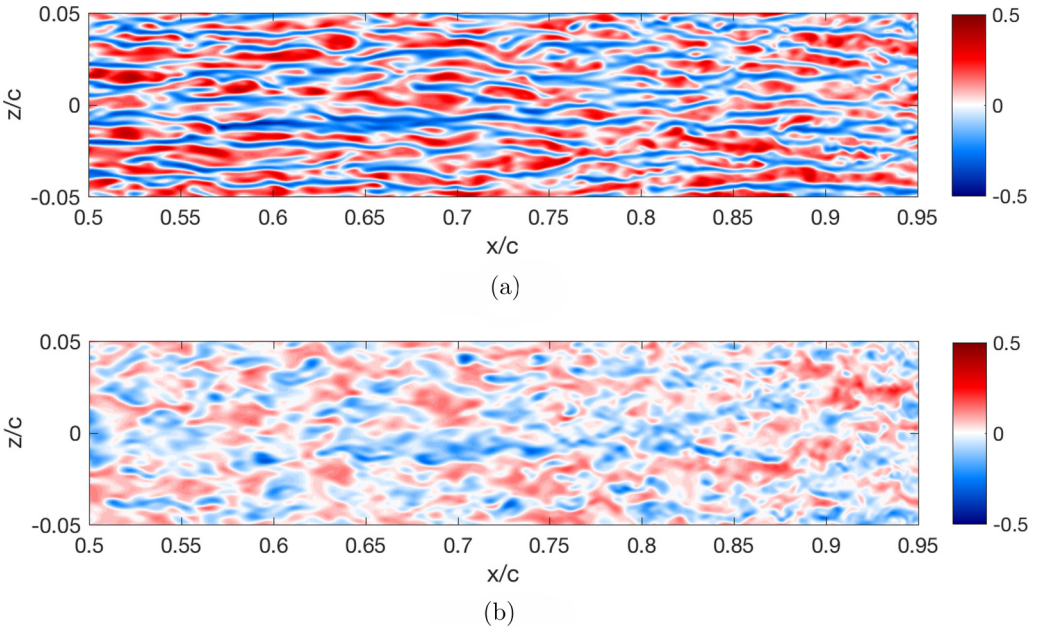

FIG. 4. Instantaneous streamwise velocity fluctuation field in the wall-parallel plane. (a) $y^+ \approx 15$ and (b) $y^+ \approx 100$.

peak of the spectral energy distribution is observed at a wall distance of $y^+ \approx 15$ for a wavelength $\lambda_z^+ \approx 150$, where $\lambda_z^+ = 2\pi/k_z^+$. This wavelength appears to be representative of the near-wall cycle signature in many studies across a range of Reynolds numbers and flow types (see, for

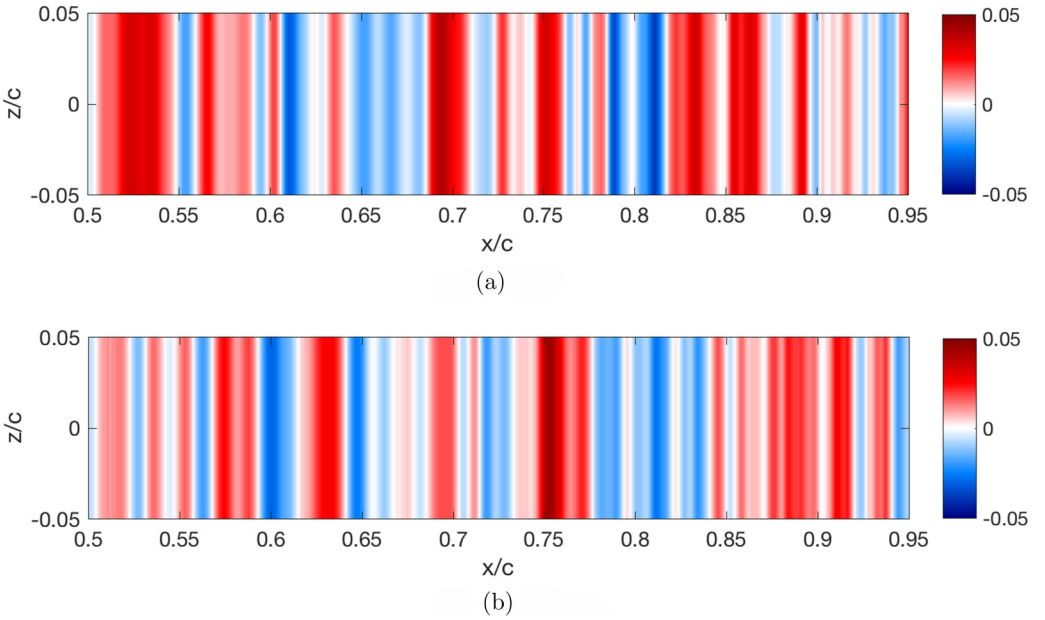

FIG. 5. Spanwise averaged velocity fluctuations. (a) $y^+ \approx 15$ and (b) $y^+ \approx 100$.

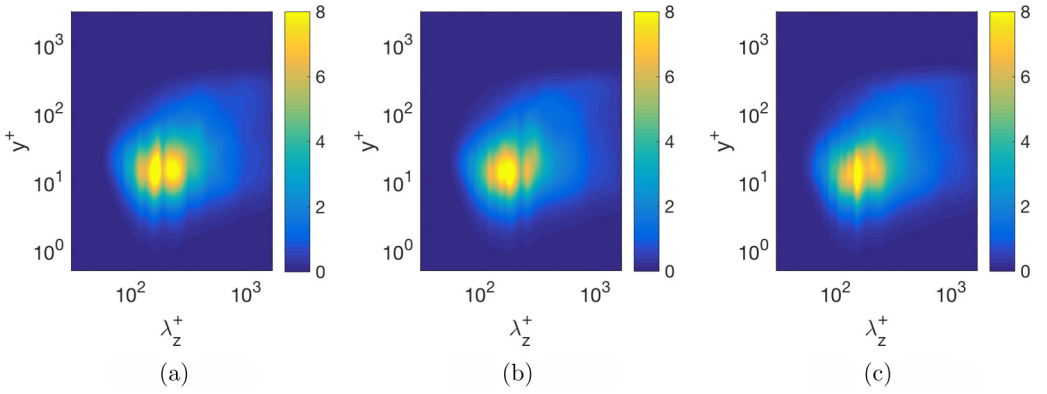

FIG. 6. Spanwise premultiplied power spectral density of the streamwise velocity u, $k_z E_{uu}$, at three different stations of the profile. (a) $x/c = 0.7$, (b) $x/c = 0.8$, and (c) $x/c = 0.9$.

instance, Ref. [41]), which corresponds to the characteristic streak spacing in wall turbulence. The overall shape of the spectra is consistent with turbulent boundary layers; oscillations observed in wave-number spectra contours may be related to the finite spanwise extent or to the finite number of time steps in the database.

To also show the wave number $k_z^+ = 0$, which corresponds to $\lambda_z^+ \to \infty$ and consequently does not appear in the plot, the spanwise power spectral density, without premultiplication, is shown in Fig. 7. The wave number $k_z^+ = 0$ corresponds to two dimensional perturbations, such as the ones isolated in Fig. 5, which are little explored in the literature and is the main focus in this study.

It is interesting to consider two-dimensional spectra in a λ_t-λ_z plane, where λ_t denotes the period of oscillation. The two-dimensional spectral information is shown for the streamwise velocity at stations $x/c = 0.7$, $x/c = 0.8$, and $x/c = 0.9$ in Fig. 8 for the wall-normal positions $y^+ \approx 15$ and $y^+ \approx 100$. Again, the footprint of the near-wall streaks is obvious at $y^+ \approx 15$, when moving away from the wall, the range of energy containing scales changes, but the near-wall peak remains significant across the whole boundary layer at about $\lambda_t^+ \approx 100$ and $\lambda_z^+ \approx 100$. The red dashed line in Fig. 8 represents $\lambda_a^+ = c_0/u_\tau \lambda_t^+$, where λ_a^+ is the acoustic wavelength, c_0 is the sound speed and u_τ is the friction velocity. This line delimits the propagative and evanescent regions in the graphic, indicated by letter P and E respectively, such that above this line the waves are always propagative (supersonic phase speed in the spanwise direction) and below they are always evanescent (subsonic spanwise phase speed).

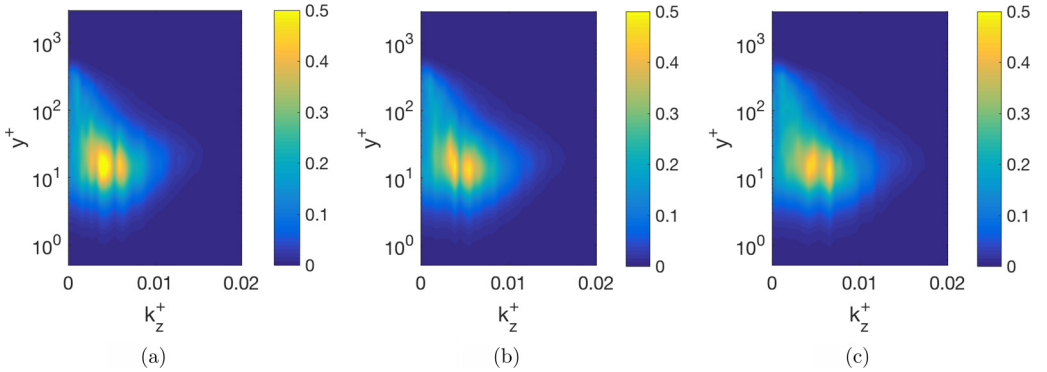

FIG. 7. Spanwise power spectral density of the streamwise velocity u at three different stations of the profile. (a) $x/c = 0.7$, (b) $x/c = 0.8$, and (c) $x/c = 0.9$.

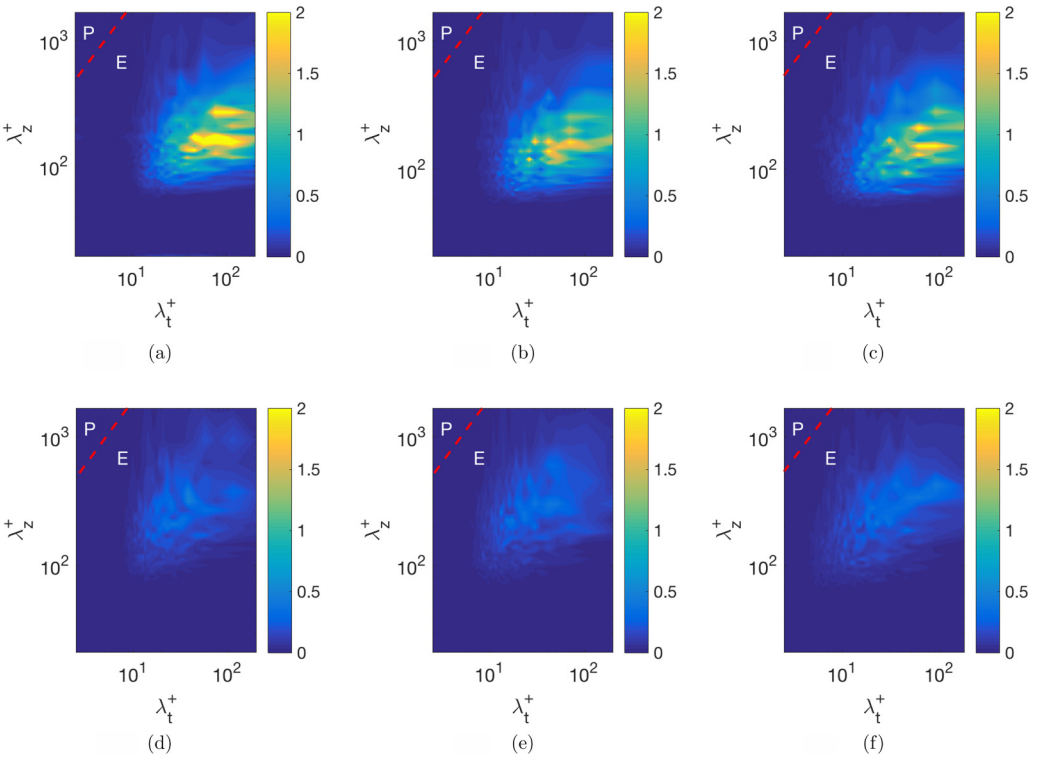

FIG. 8. Two-dimensional premultiplied energy spectrum, $k_z\omega E_{uu}(\lambda_z, \lambda_t)$, of the streamwise velocity for wall-normal positions $y^+ \approx 15$ at (a) $x/c = 0.7$, (b) $x/c = 0.8$, and (c) $x/c = 0.9$, and for $y^+ \approx 100$ at (d) $x/c = 0.7$, (e) $x/c = 0.8$, and (f) $x/c = 0.9$. The red dashed line represents the $\lambda_a^+ = c_0/u_\tau \lambda_t^+$, which delimits the propagative (P) and evanescent (E) regions.

The wave number $k_z^+ = 0$ (or $\lambda_z^+ \to \infty$) corresponds to two dimensional perturbations, which are always related with propagative waves. The streaky structures present in the flow, which dominate the turbulent kinetic energy, correspond to the peak region in the premultiplied energy spectrum around $\lambda_t^+ \approx 100$ and $\lambda_z^+ \approx 100$; hence, they lead only to evanescent waves and do not radiate noise, despite their high amplitude. Thus, when one is interested in trailing-edge noise, the dominant turbulent features might not be the most relevant for sound radiation. This will be further investigated in the next section.

IV. FLOW-ACOUSTIC CORRELATIONS

We present in this section the results of flow-acoustic correlations to discern the regions in the flow most relevant for sound radiation. As usual in computations of turbulent flows, the simulation attempts to represent an infinite-span airfoil by considering periodic boundary conditions at the spanwise extremities. This spanwise periodicity leads to *discrete* values of the spanwise wave number k_z, given as

$$k_z c = \frac{2\pi n}{L_z} c, \tag{1}$$

where n is an integer number and L_z is the length of the computational domain in the spanwise direction. The simulation domain has $L_z = 0.1c$; the same spanwise length was used in the NACA 4412 simulations by Ref. [42]. The boundary layer thickness δ at $x/c = 0.9$ is equal to $0.0311c$. L_z

corresponds thus to about 3 boundary layer thicknesses at $x/c = 0.9$, and was seen by Ref. [37] to be sufficient to obtain a decaying two-point coherence along the span. With this computational domain, besides the two-dimensional mode $k_z = 0$ the first nonzero wavelength corresponds to $\lambda_z/c = 0.1$, which is small in terms of the airfoil chord, but large in terms of the boundary layer thickness ($\lambda_z/\delta = 3.2154$).

To determine flow-acoustic correlations flow fluctuations were taken throughout a body-fitted O-grid block (Fig. 1, referenced as *grid 1*). Fluctuations at all these positions were correlated with a representative position in the acoustic field, aligned with the trailing edge, at $x/c = 1$ and $y/c = 1$. The use of numerical data has the advantage of allowing the study of correlations using different quantities, taken at various positions in the flow. Moreover, it is possible to apply a preliminary Fourier decomposition in the spanwise direction, which is appropriate given the homogeneity in z. The dependence of trailing-edge scattering on spanwise wave number was studied by Ref. [25], who have shown, using a Fourier transform applied to the tailored Green's function of Ref. [4], that only spanwise wave numbers satisfying $k_z < k$, where $k = \omega/a_0$ is the acoustic wave number, lead to far-field sound; the two-dimensional mode, $k_z = 0$, satisfies this condition for all frequencies.

The numerical simulation has a duration of $ta_0/c = 15.98$, which was seen in Ref. [37] to be sufficient to converge statistics that were subsequently validated with experimental data. This duration is small compared to usual time series taken from experiments, with a consequent impact in the calculation of flow-acoustic correlations. The clearest effect of this is an overall noise level in the correlations, whose order is 15%. It will be shown nonetheless that for some positions the correlation peaks greatly exceed the background noise, and thus can be interpreted as a meaningful relation between fluctuations in the turbulent flow and the radiated sound.

A. Two-dimensionality and antisymmetry of the acoustic field

A first observation of the radiated sound can be made with regard to the power spectral density (PSD) in the acoustic field. Besides the usual single point PSD based on pressure $p(x = c, y = c, z = 0, t)$, to evaluate the frequency range for which the acoustic field can be considered as two-dimensional it was also computed the PSD of the spanwise-averaged pressure, denoted as $p(x = c, y = c, k_z = 0, t)$, corresponding to $k_z = 0$. Another expected feature of the acoustic field is its antisymmetric nature, which is predicted by theory [4]. Since the present study is dealing with flow at zero angle of attack around a symmetric airfoil, it is natural to decompose the pressure in even and odd parts with respect to $y = 0$, p_e and p_o respectively, leading to

$$p_e(x, y, k_z = 0, t) = \frac{p(x, y, k_z = 0, t) + p(x, -y, k_z = 0, t)}{2}, \tag{2a}$$

$$p_o(x, y, k_z = 0, t) = \frac{p(x, y, k_z = 0, t) - p(x, -y, k_z = 0, t)}{2}, \tag{2b}$$

such that $p = p_e + p_o$. Theory thus predicts a dominance of the antisymmetric field p_o [7]. Power spectra of the single-point pressure, of the spanwise-averaged pressure, and of its even and odd parts are shown in Fig. 9.

Vertical lines in Fig. 9 show cut-on values of He for the successive spanwise wave numbers according to the analysis of Ref. [25]:

$$\mathrm{He}_n = k_n c = \frac{2\pi n}{L_z} c, \tag{3}$$

Helmholtz numbers satisfying $\mathrm{He} > \mathrm{He}_n$ (i.e., to the right of the corresponding vertical line) are such that the nth spanwise wave number in the source is propagative. However, if $\mathrm{He} < \mathrm{He}_n$ (left of the corresponding line) the nth spanwise wave number leads solely to evanescent waves. The two-dimensional mode $k_z = 0$, or $n = 0$, is propagative for all He.

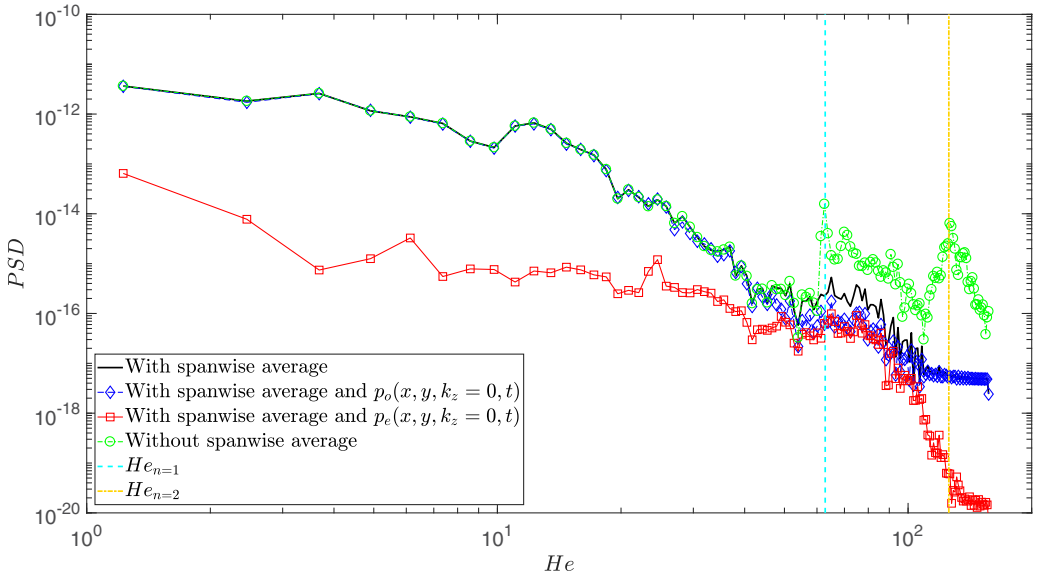

FIG. 9. Power spectral densities of pressure at $x/c = 1$ and $y/c = 1$.

Note that there is virtually no difference between spectra with and without spanwise averaging up to He corresponding to the cut-on condition for $n = 1$, which is consistent with the theoretical analysis. Above that value some differences appear, but the energy-containing part of the acoustic spectrum is clearly two-dimensional. It is interesting to notice that above the cut-on He for $n = 2$ a new peak also emerges in the PSD. Due to the filtering procedure of the large-eddy simulation, which retains only the larger turbulent scales, it was not possbile to determine the relevance of these high-frequency peaks. For our purposes, it is sufficient to observe that the bulk of the acoustic spectrum consists solely of two-dimensional disturbances.

These results are in line with the theory presented by Ref. [25], and suggest that the predominantly two-dimensional acoustic field is generated by corresponding two-dimensional flow fluctuations. In a similar manner to the approach of Ref. [34], who obtained more significant flow-acoustic correlation for jets when the axisymmetric mode was isolated, we compare in what follow the usual two-point statistics with correlations between spanwise averages of turbulent and acoustic fields.

Figure 9 also shows that the spanwise-averaged pressure field is almost entirely antisymmetric, as the PSD of odd component p_o is very close to the spanwise average, and the even component p_e is about two orders of magnitude lower for the energy-containing part of the spectrum. This property will also be explored in the next section, since the antisymmetric part of turbulent and acoustic fields can also be isolated prior to flow-acoustic correlations.

B. Correlations between pressure in the near and acoustic fields

The evaluation of correlation coefficients is started by looking solely at pressure fluctuations, with correlations between near-field and acoustic pressure. A sample correlation of surface pressure at $x/c = 0.97$ and far-field pressure at $x/c = 1.0$ and $y/c = 1.0$ is shown in Fig. 10. For both positions we consider the spanwise averaged pressure, due to the arguments presented in Secs. III and IV A. Some correlation noise is present, leading to oscillations within ± 0.2 in the correlation coefficient; this is due to the duration of the time series from the simulation. There is nonetheless a clear peak, with correlation coefficient of about 0.55, well above the noise level. The peak occurs at

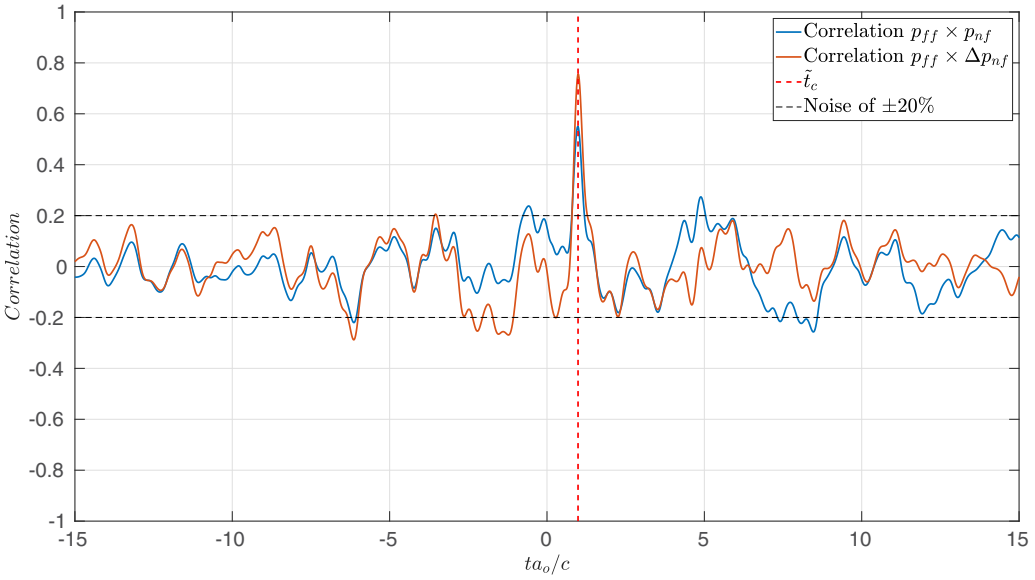

FIG. 10. Correlation coefficient of surface pressure at $x/c = 0.97$, and far-field pressure at $x/c = 1.0$ and $y/c = 1.0$. The correlation $p_{ff} \times p_{nf}$ (far-field pressure, p_{ff}, and near-field pressure, p_{nf}), indicated by (——), is calculated with the far-field pressure fluctuation at $x/c = 1.0$ and $y/c = 1.0$ and correlated with wall pressure fluctuation at $x/c = 0.97$; correlation of $p_{ff} \times \Delta p_{nf}$, indicated by (——) is computed between far-field pressure fluctuation and wall pressure difference between upper an lower surface at the same location.

the expected nondimensional time of sound propagation, given by

$$\tilde{t} = \frac{c}{1 + M_\infty \cos\theta}. \tag{4}$$

This ensures that the observed correlation peak is not spurious, and should be related to trailing-edge noise.

For a global view of the peak correlation coefficients, the near-field pressure is taken for all points in the numerical grid around the airfoil, and the acoustic pressure is taken at $x/c = 1.00, y/c = 1.00$, the same position considered in the results of Fig. 10. The peak correlation coefficient between spanwise-averaged near-field and acoustic pressure is shown in Fig. 11. Due to the characteristic

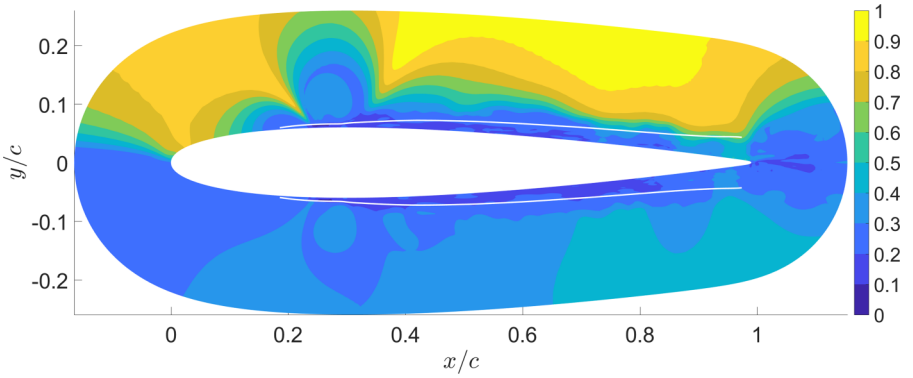

FIG. 11. Peak correlation between *grid 1* pressure and far-field pressure. Both quantities are spanwise averaged.

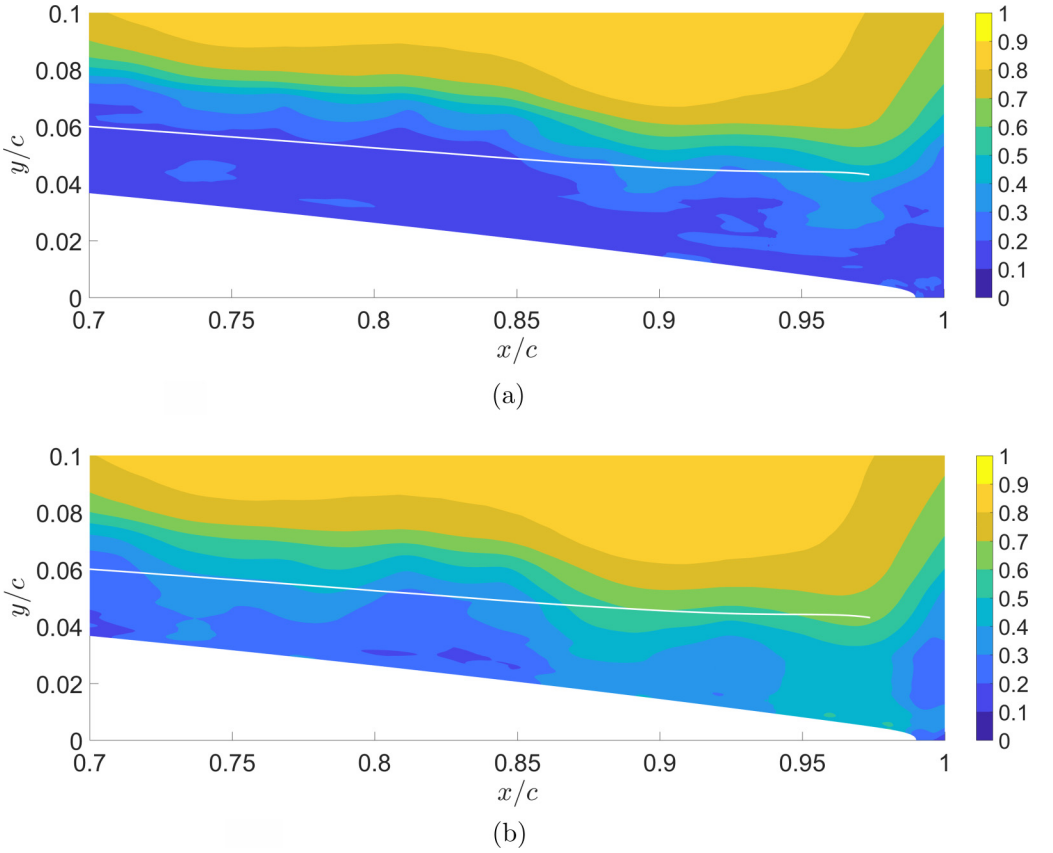

FIG. 12. Peak correlation coefficient between near-field pressure in the trailing-edge region and acoustic pressure. (a) Correlation between the quantities without spanwise-average and (b) Correlation between spanwise-averaged quantities.

noise level of 20% in the correlation coefficients, seen in Fig. 10, peak values should only be considered as meaningful when well above 0.2. To aid the analysis the boundary-layer thickness was plotted in the trailing-edge region. Determination of the boundary layer thickness close to the trailing edge becomes difficult due to the significant gradients of the outer velocity, only values of δ up to $x/c \approx 0.94$ are shown.

There is a significant correlation peak in outer portions of the figure, but this occurs outside the boundary layer, and is hence attributed to correlations between an acoustic wave, that has already left the turbulent boundary layer, and the far-field pressure. The relevant flow-acoustic correlations should be sought for a near-field position within the boundary layer or the wake. A zoom of Fig. 11(a) in the trailing-edge region is shown in Fig. 12(a). One can observe high correlation peaks inside the boundary layer, extending all the way from the wall to the boundary layer thickness δ. The correlation coefficients are roughly 0.5 near the trailing edge. However, the standard two-point correlations, where spanwise averages of the pressure are not taken, do not display visible peaks above the noise level, as shown in Fig. 12(b). This result agrees with the theoretical considerations of [25], showing that higher correlations are obtained when $k_z = 0$ is isolated in the turbulent field. For the energy-containing part of the acoustic spectrum only the two-dimensional mode is radiating, as seen in the previous section. Furthermore, one can observe that the source of sound is concentrated in the neighborhood of the trailing edge (centered around $x/c = 0.96$), which is also expected [4].

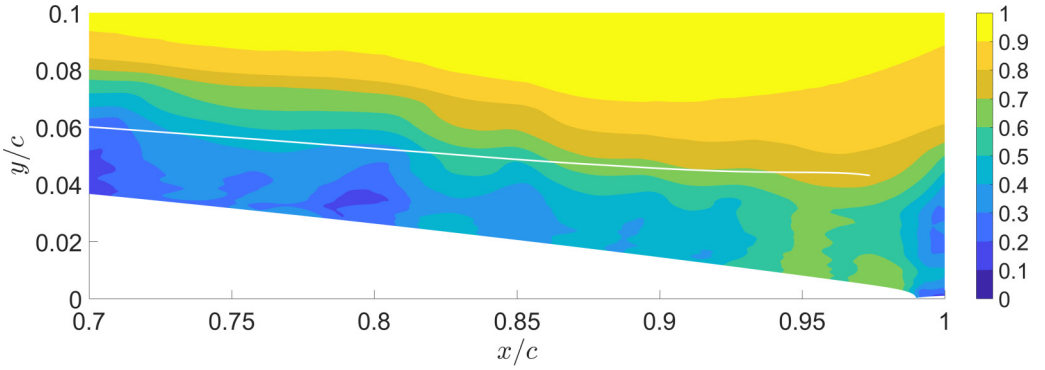

FIG. 13. Peak correlation between *grid 1* pressure difference of the upper and lower surface of the airfoil and far-field pressure; spanwise-averaged quantities.

It was seen that taking spanwise averages of flow fluctuations greatly enhances the correlation coefficients. If now it is considered that trailing-edge scattering occurs due to advected disturbances in both upper and lower airfoil surfaces, then it makes sense to extract the difference between upper- and lower-surface fluctuations prior to the calculation of correlations. The underlying idea is that identical disturbances at both sides of the trailing edge would lead to destructive interference and hence low acoustic scattering. The antisymmetric pattern seen in the radiated pressure in the previous section would thus occur of antisymmetric disturbances advecting past the trailing edge.

This idea is pursued in Fig. 13, where we shown the correlations of the pressure difference between upper and lower surfaces of the airfoil with the acoustic pressure; spanwise-averaged quantities were taken. Similar to the results previously presented, high correlations inside the boundary layer and close to the trailing edge are observed. This time correlation coefficients are even higher, getting close to approximately 0.7. The correlation peaks at the expected propagation time, as exemplified in Fig. 10.

It was seen that correlation coefficients are greatly increased if spanwise averages and differences between upper and lower surfaces are taken in the near-field, prior to the determination of correlations. This suggests that the relevant sound-producing fluctuations are two-dimensional and in phase opposition in the trailing-edge region. This will be further pursued in the next section, where velocity-pressure correlations are shown.

C. Velocity-pressure correlations

Results of the preceding section were of pressure-pressure correlations. Since velocity disturbances are more often studied in analyses of the turbulent field, and are closely related to the source terms in acoustic analogies, similar correlations are presented here, this time taken between components of the velocity vector with acoustic pressure.

The velocity-pressure correlations, using the streamwise velocity (u) component, show mainly negative peaks, which correspond to phase opposition between the two quantities. To quantify these negative peaks, Fig. 14(a) shows the *minimum* of flow-acoustic correlation, again with a prior spanwise average of fluctuations. To facilitate the comparison with figures of maximal correlation, the minimal were plotted using a reversed scale. A thin region is observed within the boundary layer in the neighborhood of trailing edge, with high correlation (in absolute value) with the radiated sound, albeit with a lower magnitude than what was seen in pressure-pressure correlations. When the spanwise average is not taken, the correlation coefficients become negligible, as shown in Fig. 14(b). This again shows that the two-dimensional part of the turbulent field is most relevant for sound radiation.

If the difference of the u-component between upper and lower surfaces is taken before correlation, leading to the antisymmetric part of the velocity field in the region around the edge, then

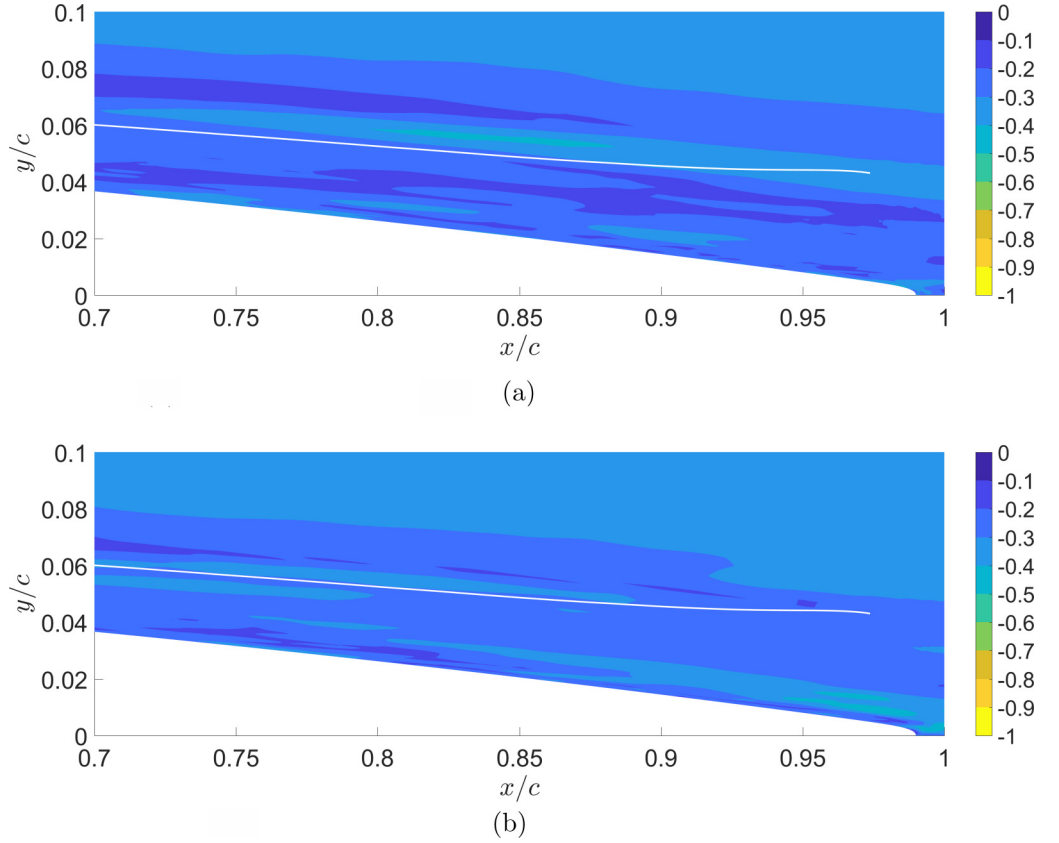

FIG. 14. Peak negative correlation between u-component and acoustic field pressure. Peak negative correlation is plotted in a reversed scale to allow direct comparison with the color scales of Fig. 12 and other similar plots. (a) Correlation between the quantities without spanwise-average and (b) Correlation between spanwise-averaged quantities.

the results of Fig. 15 are obtained. As was observed with the pressure, the correlation coefficients become more significant in the vicinity of the trailing edge. A region of significant correlation extends from $x/c = 0.8$ to $x/c = 1$. This elongated region suggests that turbulent structures advect over a significant region of the boundary layer maintaining their coherence, prior to trailing-edge scattering.

The two-dimensional part of the boundary-layer fluctuations is the most correlated with the acoustic pressure, in spite of its relative low kinetic energy. This is shown in Fig. 16, which compares the root-mean-square (RMS) of the u-component near the airfoil. We observe that downstream of the laminar-turbulent transition, in a region with approximately $0.2 \leqslant x/c \leqslant 1.2$, $\mathrm{RMS}(u_{2D}) \ll \mathrm{RMS}(u_{3D})$. The two-dimensional part of the velocity field is thus a small fraction of the overall turbulence; however, these low-amplitude two-dimensional structures are closely related with trailing-edge noise.

V. SPECTRAL PROPER ORTHOGONAL DECOMPOSITION

A. Methodology

POD was first introduced by Lumley (1967) and consists in finding, within an ensemble of realizations of the flow field, orthogonal basis functions that maximize the mean square energy

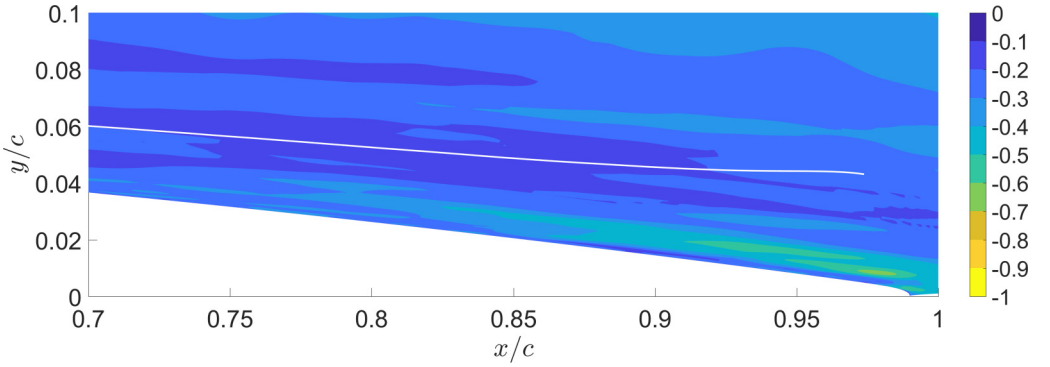

FIG. 15. Minimum correlation between *grid 1* u-component, with difference between the upper and lower surfaces of the airfoil, and acoustic field pressure. Fluctuations were spanwise averaged. See comments in the caption of Fig. 14.

[43]. In this study, POD in the frequency domain, or SPOD [32], was employed to analyze the numerical LES data, following the procedure outlined by [35].

Prior to the SPOD, we apply a spanwise Fourier transform of the fluctuations. Since the LES uses periodic boundary conditions in the spanwise direction z, the span can be considered as a homogeneous direction and Fourier modes in z become the optimal orthogonal basis functions in this direction [43]. Focus is given on the two-dimensional mode, which is most relevant for low-frequency trailing-edge noise, as seen in the previous section. Accordingly, in what follows it is implicit that a spanwise average has been taken for all flow quantities, which no longer have a z-dependence.

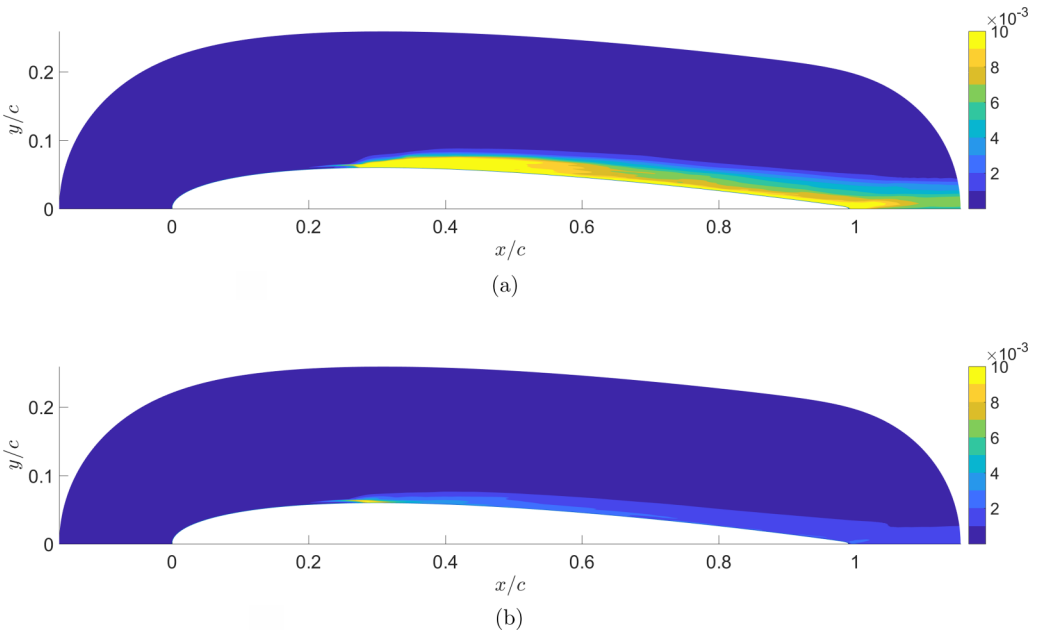

FIG. 16. Comparison between the RMS of *grid 1* u-component without and with spanwise-averaging. (a) RMS of *grid 1* u-component without spanwise-average and (b) RMS of *grid 1* u-component with spanwise-average.

A further decomposition can be applied to the fields prior from computation of SPOD modes. Since the present study is dealing with a symmetric airfoil at zero angle of attack, the flow along upper and lower surfaces of the airfoil should have the same statistics; accordingly, fluctuations can be split into parts that are even (symmetric) or odd (antisymmetric) with respect to the airfoil chord, similarly to what was done for the acoustic pressure in Eq. (2). The full field is a sum of symmetric an antisymmetric parts. Since acoustic radiation by trailing edges was seen to be antisymmetric in Sec. IV A, focus is given on pressure disturbances p and streamwise velocity fluctuations u which are odd with respect to $y = 0$; the vertical velocity v must in turn be symmetric to satisfy the continuity equation. Odd and even parts of a given variable are given as in Eq. (2). Due to the antisymmetric nature of the acoustic radiation, seen in Sec. IV A, and the underlying linearity of SPOD, only antisymmetric modes (in u and p) are expected to have significant support in the acoustic field.

In the present study, SPOD is applied to velocity components u and v to extract the turbulent kinetic energy; pressure p is also retained in the SPOD modes, as will be discussed later. First, a Fourier transform is performed to the velocity and pressure fields in time to obtain the field for a specific frequency ω, $\hat{\mathbf{q}}(x, y, \omega)$ (where hats denote Fourier-transformed quantities); then it is applied the SPOD to this transformed field, which amounts to solving the integral equation

$$\int R(\mathbf{x}, \mathbf{x}', \omega)\mathbf{\Phi}(\mathbf{x}', \omega)d\mathbf{x}' = \lambda(\omega)\mathbf{\Phi}(\mathbf{x}, \omega), \tag{5}$$

where $\mathbf{\Phi}$ represents the basis functions (SPOD modes), λ is the corresponding eigenvalue and R is the two-point cross-spectral density. R is Hermitian, and thus eigenvalues are real and eigenfunctions are orthogonal. Since the number of grid points is high, it is more efficient to use the snapshot method, where the eigenvalue problem is replaced by

$$A(\omega)\boldsymbol{\xi} = \lambda\boldsymbol{\xi}, \tag{6}$$

where $\boldsymbol{\xi}$ is an auxiliary eigenfunction, and elements of matrix A are given as

$$A_{i,j}(\omega) = \langle \hat{\mathbf{q}}_i(x, y, \omega), \hat{\mathbf{q}}_j(x, y, \omega) \rangle, \tag{7}$$

where $\hat{\mathbf{q}}_i(x, y, \omega)$ refer to the ith realization of the Fourier transformed variables (in practice taken as a short-time Fourier transform of the ith block of the time series) and $\langle \cdot, \cdot \rangle$ is the inner product

$$\langle \hat{\mathbf{q}}_i(x, y, \omega), \hat{\mathbf{q}}_j(x, y, \omega) \rangle = \iint (\hat{u}_i^*(x, y, \omega)\hat{u}_j(x, y, \omega) + \hat{v}_i^*(x, y, \omega)\hat{v}_j(x, y, \omega))dxdy. \tag{8}$$

Once the auxiliary eigenfunctions $\boldsymbol{\xi}$ are found, SPOD modes are obtained as

$$\mathbf{\Phi}^{(n)}(\mathbf{x}) = \frac{1}{N_b\lambda^{(n)}} \sum_{k=1}^{N_b} \xi_k^{(n)} \hat{\mathbf{q}}_k(\mathbf{x}), \tag{9}$$

where N_b is the total number of blocks and $\xi_k^{(n)}$ refers to the kth component of the nth eigenfunction, with k ranging from 1 to N_b. Notice that even though only the velocity components are considered in the inner product in Eq. (8), which is consistent with the incompressible turbulent kinetic energy, the SPOD mode includes the pressure, as it is reconstructed by Eq. (9) with flow realizations that also include short-time Fourier transforms of the pressure. This will be useful to examine the contributions of the SPOD modes to the radiated sound.

The short-time FFTs required for SPOD have been taken considering blocks of 128 snapshots with 75% overlap, leading to a total number of blocks of $N_b = 22$. SPOD is calculated numerically using the approach described by Ref. [44]. The decreasing ordering of the eigenvalues and eigenvectors ensures that the most important modes in terms of energy are the first modes. This usually means that the first modes will be associated with large scale flow structures. If the flow has dominant flow structures, then these are therefore reflected in the first SPOD modes. In the present study focus is given on five different frequencies He $\approx$ 4.95, 7.42, 12.37, 17.32, and 22.26.

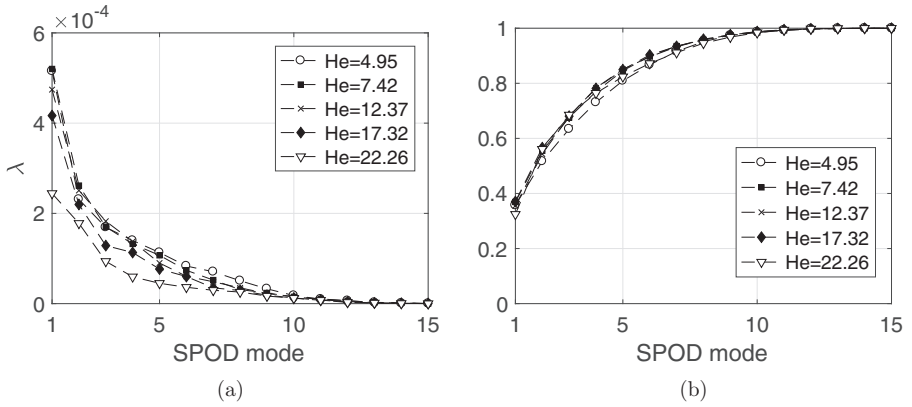

FIG. 17. (a) SPOD eigenvalues; (b) cumulative contribution of SPOD modes to total TKE.

The lower frequency is representative of the peak trailing-edge radiation, as shown in Fig. 2. The convergence of SPOD was studied, and the leading two modes were considered as converged. Results are shown in the Appendix.

B. SPOD results for velocity

SPOD eigenvalues are shown in Fig. 17(a) and the cumulative contribution of the SPOD modes to the total turbulent kinetic energy (TKE) is shown in Fig. 17(b). The convergence of SPOD eigenvalues is relatively fast; one can see that approximately 37% of the total TKE can be reconstructed using just the first SPOD mode for He = 4.95, 7.42, 12.37, and 17.32, and about 33% for He = 22.26. The six first SPOD modes represent more than 87% of the total energy in all frequencies. Notice that these results are for spanwise-averaged fluctuations, considering the antisymmetric mode for u and p, and symmetric mode for v, as discussed previously. Further, details about the statistical convergence of SPOD are in the Appendix.

The SPOD results will be presented for the first and second mode, since those are reasonably converged for the frequencies studied here, according to the normalized projection coefficient β in Fig. 23. Figure 18 shows the first SPOD mode for streamwise velocity fluctuations u and chord-normal velocity fluctuations v for all analyzed frequencies. Figure 19 shows the second SPOD mode for streamwise velocity fluctuations u and chord-normal velocity fluctuations v for all analyzed frequencies. SPOD modes are complex-valued, and the real part is plotted. Due to the symmetry of the problem, just the airfoil upper surface is plotted. Results are plotted starting from the boundary layer tripping towards shortly after the trailing edge, since, in all cases, there are negligible fluctuations at the leading edge region, where the boundary layer is laminar.

The first and second SPOD modes, Figs. 18 and 19 respectively, show a coherent wave from the boundary-layer tripping until the trailing edge. There are pronounced amplitudes at the transition region, due to artificial suction and blowing between $x/c = 0.15$ and $x/c = 0.2$. In downstream stations the coherent wavy structure persists, even within a region of developed turbulent boundary layer, as studied in Sec. III. Analysis of real and imaginary parts of the SPOD mode reveals that this is an advecting hydrodynamic wave. In the present study focus is given to the trailing-edge region, which plays an important role to sound radiation. For the first and second SPOD modes pronounced amplitudes are presented at the trailing-edge region for the lowest frequencies He = 4.95, 7.42, and 12.37, see Figs. 18(a)–18(f) and 19(a)–19(f). For the highest frequencies He = 17.32 and He = 22.26, one can see in Figs. 18(g)–18(j) that, after the boundary layer tripping, the coherent waves attenuate as they reach the trailing edge. However one can notice that the amplitudes of

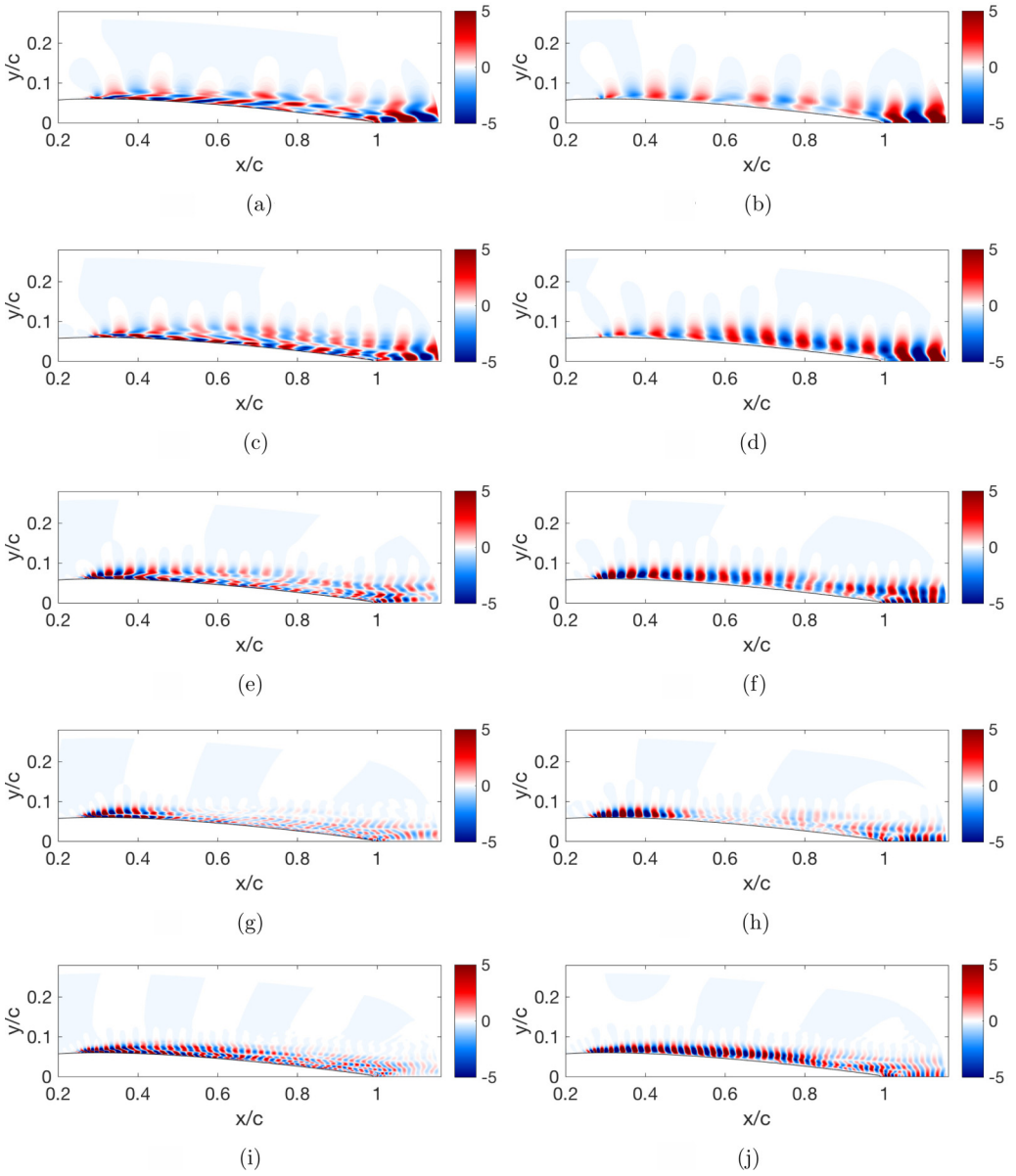

FIG. 18. SPOD mode 1. (a) Φ_u at He = 4.95, (b) Φ_v at He = 4.95, (c) Φ_u at He = 7.42, (d) Φ_v at He = 7.42, (e) Φ_u at He = 12.37, (f) Φ_v at He = 12.37, (g) Φ_u at He = 17.32, (h) Φ_v at He = 17.32, (i) Φ_u at He = 22.26, and (j) Φ_v at He = 22.26.

coherent hydrodynamic waves are slightly more pronounced in the second SPOD mode, shown in Figs. 19(g)–19(j), but still not as pronounced as in the lowest frequencies.

The coherent wave shown in the lower frequencies of the SPOD mode appears in the trailing-edge region, even though the boundary layer is at an already developed turbulent state; this shows that once careful post-processing is performed, the turbulent boundary layer presents two-dimensional coherent structures forming a hydrodynamic wave. The trailing edge is a region of adverse pressure gradient in the boundary layer, which is known to enhance boundary-layer instability for laminar

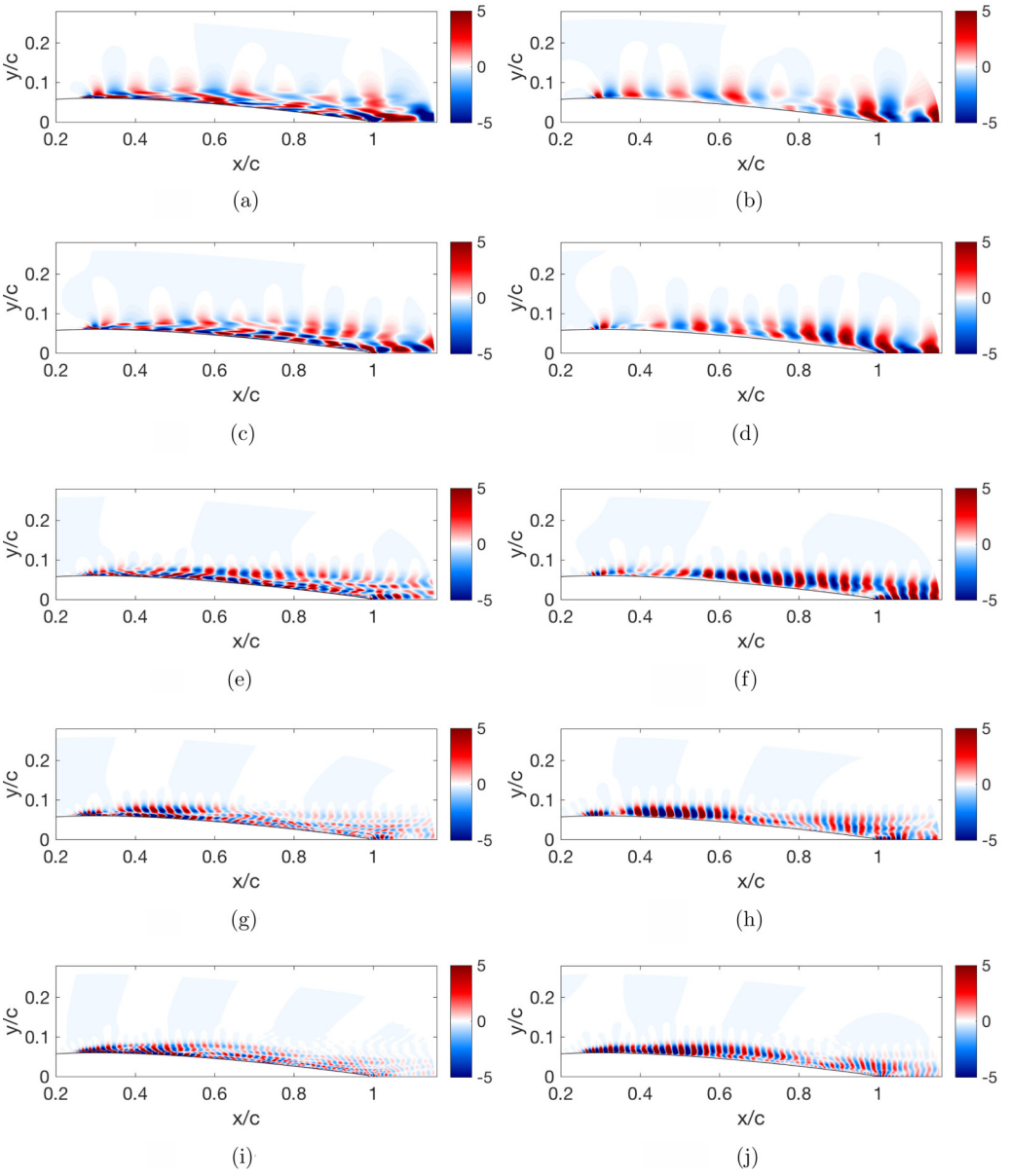

FIG. 19. SPOD mode 2. (a) Φ_u at He = 4.95, (b) Φ_v at He = 4.95, (c) Φ_u at He = 7.42, (d) Φ_v at He = 7.42, (e) Φ_u at He = 12.37, (f) Φ_v at He = 12.37, (g) Φ_u at He = 17.32, (h) Φ_v at He = 17.32, (i) Φ_u at He = 22.26, and (j) Φ_v at He = 22.26.

flows [45], and the present results suggest that a similar mechanism may be at work in the turbulent boundary layers near the trailing edge.

The SPOD results for streamwise velocity fluctuations u in all cases (see Figs. 18 and 19) show near-wall fluctuations displaying change in phase in the wall-normal direction. This suggests a behavior reminiscent of Tollmien-Schlichting waves (T-S waves) albeit in a region of turbulent boundary layer. The appearance of such waves in turbulent boundary layers dates back to [46],

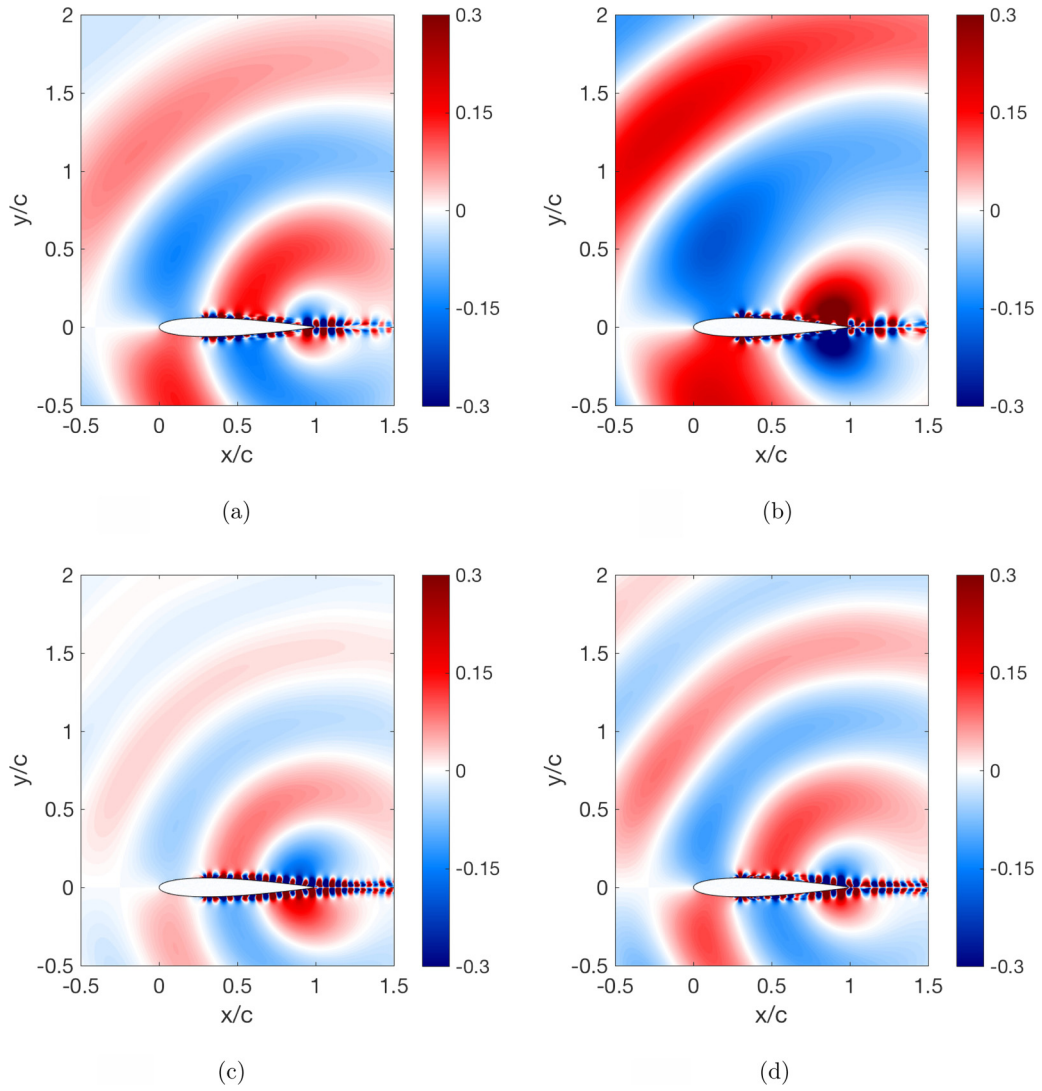

FIG. 20. First and second SPOD mode for pressure corresponding to the two lower frequencies: (a), (b) He = 4.95 and (c), (d) He = 7.42.

where turbulent flows were forced using vibrating wires; here, the natural turbulent boundary layer is seen to exhibit T-S–like waves as well.

In general all the SPOD results show the same pattern: a coherent wave propagating from the boundary layer tripping toward the trailing edge. Waves with more pronounced amplitudes at the trailing edge are noticed at the three lowest frequencies, and weaker amplitudes for the two higher frequencies.

One can notice that at He = 7.42, 12.37, 17.32, and 22.26 the SPOD results are smoother than for the lowest frequency He = 4.95. The results are more difficult to converge at low frequencies; this can be understood by noting that when time duration is short, in a given time there are fewer low frequency events. It is thus harder to converge statistics, such as SPOD modes, for the lower frequencies.

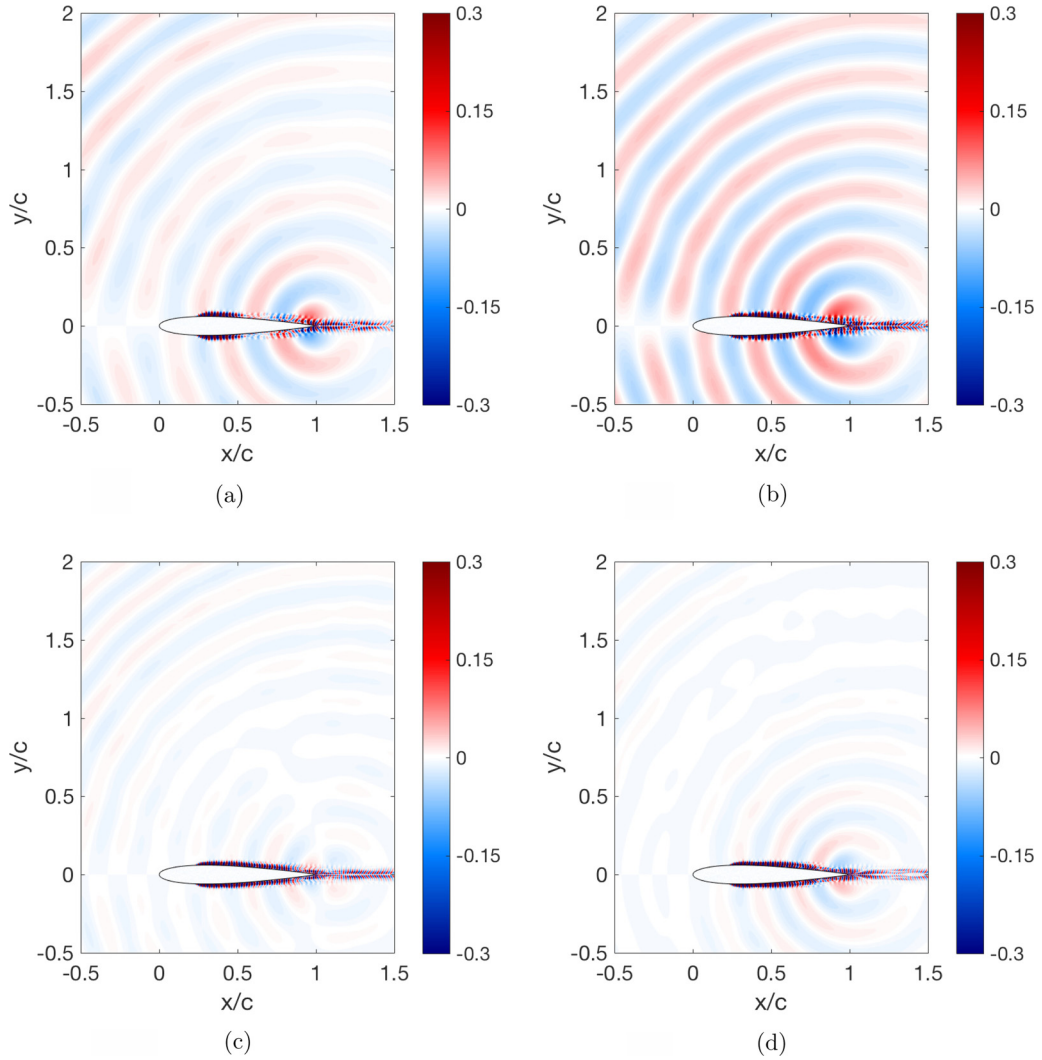

FIG. 21. First and second SPOD modes for pressure corresponding to the two higher frequencies: (a), (b) He = 17.32 and (c), (d) He = 22.26.

C. SPOD results for pressure

The pressure of the first and second SPOD modes are shown in Fig. 20, for He = 4.95 and 7.42. Besides the coherent hydrodynamic wave pattern near the airfoil surface, the radiated acoustic waves can be observed with pronounced amplitudes in those figures. As expected, the waves have an apparent origin at the trailing edge. All modes have an implicit antisymmetry at $y = 0$, as previously discussed; this antisymmetry is depicted in Fig. 20 for the visualization of the acoustic waves, which have the expected pattern for trailing-edge noise [see, for instance, Refs. 24,37].

To also analyze higher frequencies, the first and second SPOD modes for the two higher frequencies He = 17.32 and He = 22.26 are shown in Fig. 21. Here the radiated acoustic waves can also be observed, but with a much less pronounced amplitudes if compared the lower frequencies. For these Helmholtz numbers the disturbances are seen to have lower amplitudes in the trailing-edge region (see Figs. 18 and 19), which is consistent with the lower magnitude of the radiated sound.

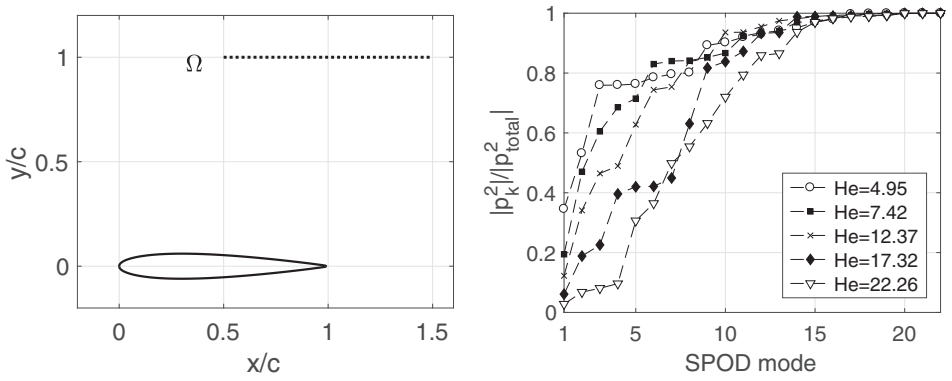

(a) (b)

FIG. 22. (a) Region of the acoustic field Ω (dashed line) used to integrate the energy representation of pressure. The continuous line represents the NACA 0012 profile. (b) Contribution of first k SPOD modes to radiated pressure on the Ω.

1. Contribution to the acoustic field

To verify how much each SPOD mode contributes to sound radiation in the acoustic field, we evaluated the cumulative contribution of k SPOD modes for the radiated pressure for points in the acoustic field. Figure 22(a) shows the region Ω where the pressure was integrated; this region is in the acoustic field, as can be seen in the SPOD-mode plots of Fig. 20. The radiated pressure p_k corresponding to the sum of k SPOD modes, integrated over Ω, was normalized by the overall pressure integrated over the same region, as

$$\frac{|p_k|^2}{|p_{\text{total}}|^2} = \frac{\int_\Omega \left(\sum_{i=1}^{k} \xi_i \phi_i\right)^2 d\Omega}{\int_\Omega \left(\sum_{j=1}^{N_b} \xi_j \phi_j\right)^2 d\Omega}. \tag{10}$$

The results of ratio $\frac{|p_k|^2}{|p_{\text{total}}|^2}$ are shown in Fig. 22(b). The first SPOD mode contributes to 35% of the total sound radiation at the lowest analyzed frequency He = 4.95, while at He = 7.42 the first SPOD mode contributes to 20%. This contribution continues dacaying with increasing frequency, to 12% at He = 12.37, 6% at He = 17.32, and 3% at He = 22.26. As in the previous analyses, these results refer solely to the two-dimensional part of the radiated pressure field; however, in Sec. IV A it was seen that the radiated sound in this simulation is almost entirely two-dimensional; hence, the first SPOD mode have substantial contributions to the acoustic radiation by the airfoil at the two lowest analyzed frequencies. When the first two modes are taken, contributions between 55% (He = 4.95) and 20% (He = 17.32) are obtained, which are significant. The highest Helmholtz number has a much slower convergence, but for the other frequencies a significant part of the radiated sound is obtained with just a pair of SPOD modes.

This result is of particular importance, since these substantial contributions of the leading SPOD modes to the radiated pressure show that with the first two SPOD modes one would recover the acoustic field within less than $3dB$ for lower frequencies. Moreover, the wavy structure of the SPOD modes shown in Figs. 18 and 19 highlights that the mechanism of sound generation is related to scattering of a coherent hydrodynamic waves advecting past the trailing edge, an observation that is in contradiction with the usual assumption that trailing-edge noise can be modeled as the scattering of *compact* turbulent disturbances [4,47–49]. Further work modeling incident disturbances at the trailing edge as convected waves appears thus to be promising.

These results complement the flow-acoustic correlations in Secs. IV B and IV C. There it was shown, using the standard time-domain correlations, that substantial correlation coefficients, up to 0.5, are obtained once the two-dimensional parts of turbulent and acoustic fields are isolated;

moreover, extracting the antisymmetric part of the turbulent field led to even higher correlations, of up to 0.7. The significant contribution of the leading SPOD modes, again obtained from the two-dimensional, antisymmetric part of the field, are consistent with the correlation results. The wavy structure of the leading SPOD modes shows that these high correlations are related to trailing-edge scattering of incident hydrodynamic waves in the turbulent boundary layer.

VI. CONCLUSIONS

In the present study we used signal processing of a large-eddy simulation, based on flow-acoustic correlations and SPOD to identify regions and mechanisms most effective to generate sound in a turbulent flow around a NACA 0012 airfoil with zero angle of attack and Mach number equal to 0.115. Earlier theoretical results for the trailing-edge noise problem, modeled using the tailored Green's function of Ref. [4], show that only wave numbers satisfying $k_z < k$, where k_z is the spanwise wave number of turbulent disturbances and k is the acoustic wave number, radiate sound [25], and based on this we seek turbulent structures satisfying this criterion in the present work. Analyses of turbulence statistics and spectra are carried out for the boundary layer close to the trailing edge, showing that two-dimensional disturbances ($k_z = 0$ or $\lambda_z^+ \to \infty$) can be isolated in the turbulent field, but with an amplitude that is one order of magnitude lower than the dominant fluctuations. It was also shown that the streaks corresponding to the peak in the premultiplied energy spectrum $\lambda_t^+ = 100$ and $\lambda_z^+ = 100$, which relates to the characteristic streak spacing in wall turbulence, are strictly silent: For the present flow the spanwise phase speeds of such structures are subsonic, and this should lead only to evanescent waves, with no contribution to the far-field sound.

With this in mind it was shown, using flow-acoustic correlations obtained using LES data, that when spanwise averages of flow fluctuations are taken, flow-acoustic correlations increase substantially. Significant correlations are obtained in the trailing-edge region for spanwise-averaged quantities: when pressure-pressure correlations were taken, a region extending from the wall to the boundary layer thickness was found to present high correlation peaks and for correlations between streamwise velocity and acoustic pressure, an elongated region closer to the wall was found to have significant correlation peaks as well, indicating that in this region there are boundary-layer structures associated with far-field sound. If the two-dimensional mode is not isolated, then correlation coefficients are lower and even negligible in some cases; this highlights that the dominant streaky structures in the turbulent boundary layer have almost no direct contribution to trailing-edge noise. Flow-acoustic correlations also increase when a difference of fluctuations between the upper and lower surfaces is taken, which agrees with theory [7] and earlier computations [15]: Convection of disturbances in phase opposition across the trailing edge (i.e., antisymmetric fluctuations) leads to maximal scattered sound, as it depends theoretically on the pressure jump over the airfoil surfaces [6].

SPOD was used in the LES database to look for coherent structures related to trailing-edge sound radiation. By doing so, it was achieved a proper separation of spatially and temporally coherent structures, which are either hidden in stochastic turbulent fluctuations or spread over a wide frequency range. We found that, in the leading SPOD mode which is statistically converged in our database, a coherent wave propagates all the way from the transition region to the trailing edge, characterizing a noncompact source, in contrast with the usual compact-eddy assumption used in early source models in acoustic analogies [4,50].

In the current work, we also explored how each SPOD mode contributes to the radiated pressure. Coherent structures in the leading SPOD modes contribute significantly to the acoustic field, up 35% for the lowest frequency studied here. The leading coherent structures captured in the first two SPOD modes correspond to a substantial amount of the radiated sound, and predictions based on the first two modes would be within 3dB of the sound pressure level for lower Helmholtz numbers. Higher frequencies were also explored in this study, and leading SPOD modes have similar wavy shape in the boundary layer, but with lower contribution to the radiated sound.

Some features of the analysis are particular to the kind of numerical simulation used here, which is an LES adopting periodic boundary conditions along the span. Other simulations use the same

approach [e.g., Refs. 16,24], and, although validation of such simulations involve a demonstration of coherence decay along the spanwise direction of the computational domain, an artifact persists: only discrete values of spanwise wave numbers are possible, and in some cases (such as in the simulation used in this work) most of the sound radiation is two-dimensional, as $k_z = 0$ is the only radiating wave number for most of the acoustic spectrum. An ongoing study from our group shows that similar two-dimensional wavy disturbances appear in numerical simulations of turbulent boundary layers over a flat plate, and do not change as the domain span is increased. However, this deserves further attention; similar turbulence studies with channel [51] and Couette flow [52] reveal that small box sizes along periodical directions tend to constrain large-scale structures in an artificial manner, and sufficiently large boxes lead to different behavior. In experiments, one should expect a much broader range of spanwise wave numbers, and nonzero k_z would probably radiate sound; the fact that the present simulation leads to results of acoustic radiation in agreement with experiments with airfoils, as seen in Fig. 2, suggests nonetheless that the two-dimensional mechanisms explored here are representative of nearly 2D, low-spanwise-wave-number turbulent structures and acoustic waves in an experimental setting. The $|k_z| < k$ condition implies that for most Helmholtz numbers only spanwise-elongated structures, with characteristic dimension greater than the acoustic wavelength, radiate sound to the far field.

Another important point deserving attention is the boundary layer tripping, which is required to force transition to turbulence at the present Reynolds number. Methods to induce transition in simulations vary and may affect boundary–layer properties further downstream [53], so the relation between tripping and coherent structures should be carefully investigated. Further numerical and experimental work aiming at the characterization of such structures is promising.

ACKNOWLEDGMENTS

The authors acknowledge the financial support received from Conselho Nacional de Desenvolvimento Científico e Tecnológico, CNPq, under Grants No. 402233/2013-1 and No. 310523/2017-6. A.V.G.C. and W.R.W. were supported by Conselho Nacional de Desenvolvimento Científico e Tecnológico, CNPq, through research scholarships. The authors also acknowledge the financial support received from Fundação de Amparo à Pesquisa do Estado de São Paulo, FAPESP, under Grant No. 2013/03413-4 and from Conselho Nacional de Desenvolvimento Científico e Tecnológico, CNPq, under Grant No. 470695/2013-7.

APPENDIX: STATISTICAL CONVERGENCE OF SPOD MODES

The convergence of the computed SPOD modes is analyzed by separating the total dataset into two blocks corresponding to 75% of the original dataset and performing the spectral POD on each subset. We compute a normalized inner product $\beta_{i;k}$ between each mode $\phi_{i;k}$ obtained with subset i and the corresponding mode ϕ_k obtained with the complete set

$$\beta_{i,k} = \frac{\langle \phi_k, \phi_{i,k} \rangle}{\sqrt{\|\phi_k\| \|\phi_{i,k}\|}}, \tag{A1}$$

where $i = (1; 2)$ indicate each subset and the same inner product of Eq. (8) is used.

The scalar quantity $\beta_{i;k}$ is the normalized projection of the kth mode of dataset and the corresponding mode of each subset. We considered as converged modes whose correlation coefficient is closest to one, meaning that the same computation with the subset leads to a mode very similar to what is obtained with the full set. This kind of analysis was also performed by Refs. [54,55]. The computed projections for $\mathrm{He} = 4.95$, 7.42, 12.37, 17.32, and 22.26 for the SPOD modes are presented in Fig. 23. It is clear from these figures that the analysis is rather sensitive to the amount of data being used, at least for the present simulation, whose time series is not long (800 snapshots). The discrepancies observed for the higher-order modes can also be attributed to modes not necessarily appearing in the same order for the two subsets. Convergence of SPOD modes is

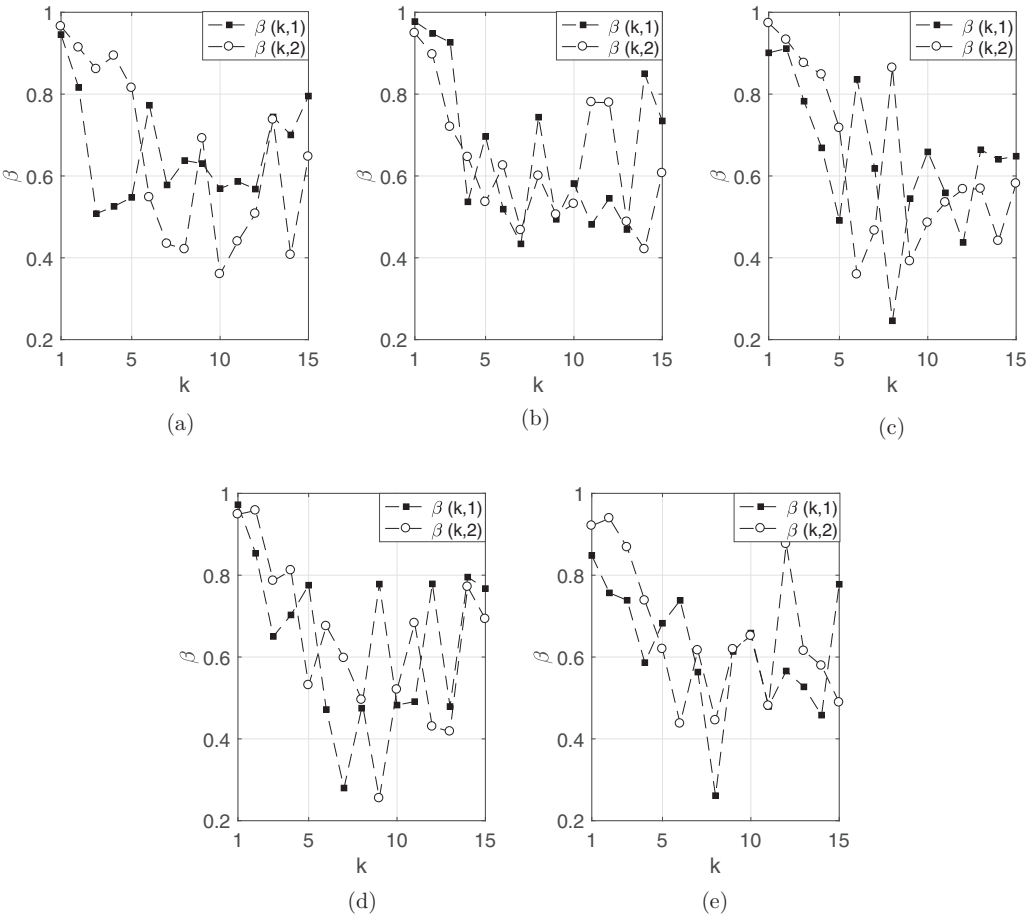

FIG. 23. Convergence of the SPOD modes, following Eq. (A1). (a) He = 4.95, (b) He = 7.42, (c) He = 12.37, (d) He = 17.32, and (e) He = 22.26.

challenging, as one deals with the two-point cross-spectral matrix. Lesshafft *et al.* [56], with a much longer time series from experimental data, only obtained 2–5 converged SPOD modes. Even so, the first two SPOD modes from the present simulation seem consistent in all cases, since different subsets lead to the same mode, with coefficients grater than 0.95 for the first mode and 0.8 for the second mode. We thus consider that the first two modes are converged and can be meaningfully analyzed.

[1] T. F. Brooks, D. S. Pope, and M. A. Marcolini, *Airfoil Self-noise and Prediction*, Vol. 1218 (National Aeronautics and Space Administration, Washington, D.C., 1989).
[2] S. Moreau and M. Roger, Effect of airfoil aerodynamic loading on trailing-edge noise sources, AIAA J. **43**, 41 (2005).
[3] D. P. Lockard and G. M. Lilley, The airframe noise reduction challenge, NASA/TM **213013**, 1 (2004).
[4] J. E. Ffowcs Williams and L. H. Hall, Aerodynamic sound generation by turbulent flow in the vicinity of a scattering half plane, J. Fluid Mech. **40**, 657 (1970).
[5] N. Curle, The influence of solid boundaries upon aerodynamic sound, Proc. R. Soc. London A **231**, 505 (1955).

[6] R. K. Amiet, Acoustic radiation from an airfoil in a turbulent stream, J. Sound Vib. **41**, 407 (1975).
[7] R. K. Amiet, Noise due to turbulent flow past a trailing edge, J. Sound Vib. **47**, 387 (1976).
[8] G. M. Corcos, The structure of the turbulent pressure field in boundary-layer flows, J. Fluid Mech. **18**, 353 (1964).
[9] M. Roger and S. Moreau, Back-scattering correction and further extensions of amiet's trailing-edge noise model. Part 1: Theory, J. Sound Vib. **286**, 477 (2005).
[10] M. S. Howe, The compact green's function for a semi-infinite elastic plate, with application to trailing-edge noise and blade-vortex interaction noise, J. Acoust. Soc. Am. **94**, 2353 (1993).
[11] B. Lyu, M. Azarpeyvand, and S. Sinayoko, Prediction of noise from serrated trailing edges, J. Fluid Mech. **793**, 556 (2016).
[12] A. Bobke, R. Vinuesa, R. Örlü, and P. Schlatter, History effects and near equilibrium in adverse-pressure-gradient turbulent boundary layers, J. Fluid Mech. **820**, 667 (2017).
[13] T. F. Brooks and T. H. Hodgson, Trailing-edge noise prediction from measured surface pressures, J. Sound Vib. **78**, 69 (1981).
[14] A. A. Oberai, F. Roknaldin, and T. J. R. Hughes, Computation of trailing-edge noise due to turbulent flow over an airfoil, AIAA J. **40**, 2206 (2002).
[15] R. D. Sandberg, L. E. Jones, N. D. Sandham, and P. F. Joseph, Direct numerical simulations of noise generated by airfoil trailing edges, in *Proceedings of the 13th AIAA/CEAS Aeroacoustics Conference (28th AIAA Aeroacoustics Conference), Rome, Italy*, AIAA Paper 2007-3469 (AIAA, Reston, VA, 2007).
[16] R. D. Sandberg and N. D. Sandham, Direct numerical simulation of turbulent flow past a trailing edge and the associated noise generation, J. Fluid Mech. **596**, 353 (2008).
[17] L. E. Jones, N. D. Sandham, and R. D. Sandberg, Acoustic source identification for transitional airfoil flows using cross correlations, AIAA J. **48**, 2299 (2010).
[18] S. J. Kline, W. C. Reynolds, F. A. Schraub, and P. W. Runstadler, The structure of turbulent boundary layers, J. Fluid Mech. **30**, 741 (1967).
[19] J. Jiménez, Near-wall turbulence, Phys. Fluids **25**, 101302 (2013).
[20] A. J. Smits, B. J. McKeon, and I. Marusic, High-Reynolds number wall turbulence, Annu. Rev. Fluid Mech. **43**, 353 (2011).
[21] J. Jiménez, Coherent structures in wall-bounded turbulence, J. Fluid Mech. **842**, P1 (2018).
[22] B. J. McKeon and A. S. Sharma, A critical-layer framework for turbulent pipe flow, J. Fluid Mech. **658**, 336 (2010).
[23] R. Moarref, A. S. Sharma, J. A. Tropp, and B. J. McKeon, Model-based scaling of the streamwise energy density in high-Reynolds-number turbulent channels, J. Fluid Mech. **734**, 275 (2013).
[24] L. E. Jones and R. D. Sandberg, Acoustic and hydrodynamic analysis of the flow around an aerofoil with trailing-edge serrations, J. Fluid Mech. **706**, 295 (2012).
[25] P. A. S. Nogueira, A. V. G. Cavalieri, and P. Jordan, A model problem for sound radiation by an installed jet, J. Sound Vib. **391**, 95 (2017).
[26] P. Holmes, J. L. Lumley, and G. Berkooz, *Turbulence, Coherent Structures, Dynamical Systems and Symmetry* (Cambridge University Press, Cambridge, 2012).
[27] M. Wei and J. B. Freund, A noise-controlled free shear flow, J. Fluid Mech. **546**, 123 (2006).
[28] J. B. Freund and T. Colonius, Turbulence and sound-field pod analysis of a turbulent jet, Int. J. Aeroacoust. **8**, 337 (2009).
[29] G. Alfonsi, L. Primavera, G. Passoni, and C. Restano, Proper orthogonal decomposition of turbulent channel flow, *Computational Fluid Dynamics 2000* (Springer, Berlin, Heidelberg, 2001), pp. 473–478.
[30] B. R. Noack, K. Afanasiev, M. Morzyński, G. Tadmor, and F. Thiele, A hierarchy of low-dimensional models for the transient and post-transient cylinder wake, J. Fluid Mech. **497**, 335 (2003).
[31] N. Aubry, P. Holmes, J. L. Lumley, and E. Stone, The dynamics of coherent structures in the wall region of a turbulent boundary layer, J. Fluid Mech. **192**, 115 (1988).
[32] C. Picard and J. Delville, Pressure velocity coupling in a subsonic round jet, Int. J. Heat Fluid Flow **21**, 359 (2000).
[33] K. Gudmundsson and T. Colonius, Instability wave models for the near-field fluctuations of turbulent jets, J. Fluid Mech. **689**, 97 (2011).

[34] A. V. G. Cavalieri, D. Rodríguez, P. Jordan, T. Colonius, and Y. Gervais, Wave packets in the velocity field of turbulent jets, J. Fluid Mech. **730**, 559 (2013).
[35] A. Towne, O. T. Schmidt, and T. Colonius, Spectral proper orthogonal decomposition and its relationship to dynamic mode decomposition and resolvent analysis, J. Fluid Mech. **847**, 821 (2018).
[36] M. Sanjose, A. Towne, P. Jaiswal, S. Moreau, S. Lele, and A. Mann, Modal analysis of the laminar boundary layer instability and tonal noise of an airfoil at Reynolds number 150,000, Int. J. Aeroacoust. **18**, 317 (2019).
[37] W. R. Wolf, J. L. F. Azevedo, and S. K. Lele, Convective effects and the role of quadrupole sources for aerofoil aeroacoustics, J. Fluid Mech. **708**, 502 (2012).
[38] W. R. Wolf, *Airfoil Aeroacoustics, LES and Acoustic Analogy Predictions* (Stanford University, Stanford, CA, 2011).
[39] D. K. Lilly, A proposed modification of the germano subgrid-scale closure method, Phys. Fluids A **4**, 633 (1992).
[40] I. Marusic, W. J. Baars, and N. Hutchins, Scaling of the streamwise turbulence intensity in the context of inner-outer interactions in wall turbulence, Phys. Rev. Fluids **2**, 100502 (2017).
[41] S. Hoyas and J. Jiménez, Scaling of the velocity fluctuations in turbulent channels up to re $\tau =$ 2003, Phys. Fluids **18**, 011702 (2006).
[42] S. M. Hosseini, R. Vinuesa, P. Schlatter, A. Hanifi, and D. S. Henningson, Direct numerical simulation of the flow around a wing section at moderate Reynolds number, Int. J. Heat Fluid Flow **61**, 117 (2016).
[43] G. Berkooz, P. Holmes, and J. L. Lumley, The proper orthogonal decomposition in the analysis of turbulent flows, Annu. Rev. Fluid Mech. **25**, 539 (1993).
[44] K. E. Meyer, J. M. Pedersen, and O. Özcan, A turbulent jet in crossflow analyzed with proper orthogonal decomposition, J. Fluid Mech. **583**, 199 (2007).
[45] P. J. Schmid and D. S. Henningson, *Stability and Transition in Shear Flows*, Applied Mathematical Sciences, Vol. 142 (Springer Science & Business Media, 2012).
[46] W. C. Reynolds and A. K. M. F. Hussain, The mechanics of an organized wave in turbulent shear flow. Part 3: Theoretical models and comparisons with experiments, J. Fluid Mech. **54**, 263 (1972).
[47] M. S. Howe, Structural and acoustic noise produced by turbulent flow over an elastic trailing edge, Proc. R. Soc. London A **442** 533 (1993).
[48] J. W. Jaworski and N. Peake, Aerodynamic noise from a poroelastic edge with implications for the silent flight of owls, J. Fluid Mech. **723**, 456 (2013).
[49] A. V. G. Cavalieri, W. R. Wolf, and J. W. Jaworski, Numerical solution of acoustic scattering by finite perforated elastic plates, Proc. R. Soc. London A **472**, 20150767 (2016).
[50] M. J. Lighthill, On sound generated aerodynamically. I. General theory, Proc. R. Soc. London A **211**, 564 (1952).
[51] J. C. Del Alamo and J. Jiménez, Spectra of the very large anisotropic scales in turbulent channels, Phys. Fluids **15**, L41 (2003).
[52] M. Lee and R. D. Moser, Extreme-scale motions in turbulent plane Couette flows, J. Fluid Mech. **842**, 128 (2018).
[53] P. Schlatter and R. Örlü, Turbulent boundary layers at moderate Reynolds numbers: Inflow length and tripping effects, J. Fluid Mech. **710**, 5 (2012).
[54] L. Lesshafft, O. Semeraro, V. Jaunet, A. V. G. Cavalieri, and P. Jordan, Resolvent-based modeling of coherent wave packets in a turbulent jet, Phys. Rev. Fluids **4**, 063901 (2019).
[55] L. I. Abreu, A. V. G. Cavalieri, and W. R. Wolf, Coherent hydrodynamic waves and trailing-edge noise, in *Prcoceedings of the 23rd AIAA/CEAS Aeroacoustics Conference*, AIAA Paper 2017-3173 (AIAA, Reston, VA, 2017).
[56] L. Lesshafft and P. Huerre, Linear impulse response in hot round jets, Phys. Fluids (1994–present) **19**, 024102 (2007).